

Optimize discrete loss with finite-difference physics constraint and time-stepping for solving incompressible flow

Yali Luo^{a,b,d}, Yiye Zou^{a,d}, Heng Zhang^{e,f}, Mingjie Zhang^d, Gang Wei^e, Jingyu Wang^{c,d,e,*}, Xiaogang Deng^d

^aSchool of Computer Science, Sichuan University, Chengdu 610065, China

^bChengdu Jincheng College, Chengdu 611731, China

^cSchool of Aeronautics and Astronautics, Sichuan University, Chengdu 610065, China

^dNational Key Laboratory of Fundamental Algorithms and Models for Engineering Simulation, Sichuan University, Chengdu 610207, China

^eSimulation and Precision Control Research Center, Taihang Laboratory, Chengdu 610213, China

^fInstitute for Aero Engine, Tsinghua University, Beijing 100084, China

arXiv:2603.07151v1 [physics.flu-dyn] 7 Mar 2026

Abstract

Computational Fluid Dynamics (CFD) is an important approach for analyzing flow phenomena and predicting engineering-relevant quantities. The governing physics is formulated as partial differential equations (PDEs) and solved numerically on computational grids. Physics-informed neural networks (PINNs) have emerged as a popular optimization-based approach for solving PDEs, but they often suffer from ill-conditioned objectives and the high cost of automatic differentiation. Optimization-based discretizations such as ODIL mitigate several PINN drawbacks by optimizing discrete variables directly, yet accuracy and efficiency remain limited on body-fitted geometries and for time-dependent problems. This paper proposes FDTO, a finite-difference time-stepping loss-optimization solver that defines physics losses from discrete residuals. FDTO couples curvilinear coordinate transforms with body-fitted structured grids and decomposes long-horizon evolution into sequential, well-conditioned subproblems consistent with time marching. The method is primarily evaluated on incompressible Navier-Stokes flows, including lid-driven cavity benchmarks, external airfoil aerodynamics (lift/drag consistency), and a cylinder case on a multi-block structured mesh with cross-block coherent solutions. Additional validations on diffusion and flow-mixing problems further demonstrate generality. Compared with representative PINN-based solvers, FDTO reduces GPU memory by about 82.6% on the lid-driven cavity case and achieves 3-5× lower relative error on the flow-mixing problem. These results indicate that FDTO enables accurate, stable, and memory-efficient discrete-loss optimization for incompressible-flow solutions, while remaining applicable to other PDE models.

Keywords: Computational Fluid Dynamics, Partial Differential Equations, Optimization-based PDE Solvers, Finite-difference Methods, Body-fitted Structured Grids, Time-stepping-oriented optimization

1. Introduction

In scientific computing and engineering, computational fluid dynamics (CFD) studies flow phenomena by formulating the governing physics as partial differential equations (PDEs). These PDEs are then solved numerically by discretizing them on computational grids, yielding algebraic systems whose solutions approximate the underlying physical behavior (Blazek, 2015). After decades of development, numerical solution methods such as the finite-difference method (FDM) (LeVeque, 2007), finite-volume method (FVM) (Moukalled et al., 2015), and finite-element method (Reddy, 1993), have achieved tremendous success (Wang et al., 2018) (Wang et al., 2020) (Chen et al., 2024a). However, traditional numerical methods often exhibit limited computational efficiency in the presence of complex geometries and boundary conditions (ZENG and ZHANG, 2025) (CAO et al., 2025).

Advances in computing hardware and data science have promoted data-driven approaches for physics-based problems.

Deep neural networks provide new opportunities for efficient PDE solvers (Lu et al., 2026). Recent studies have explored integrating neural networks with PDE methods to enhance computational performance and to learn spatiotemporal dynamics from data (Bar-Sinai et al., 2019) (Sanchez-Gonzalez et al., 2020) (Thuerey et al., 2020). Yet the increasing prevalence of noisy or incomplete data, together with the high cost of high-quality datasets, calls for more flexible and robust solution strategies (Chen et al., 2024b).

In recent years, optimization-based PDE solvers that minimize scalar objectives have attracted substantial attention. In this paradigm, unknown fields can be parameterized by neural networks and optimized by minimizing residual-based objectives, as in physics-informed neural networks (PINNs) (Raissi et al., 2019), or treated as discrete degrees of freedom and optimized directly through discrete residual losses, as in discrete-loss optimization (ODIL) (Karnakov et al., 2024).

PINNs provide a mesh-free paradigm for solving PDEs and can be trained without labeled solution data by enforcing governing equations and boundary/initial conditions through a physics-informed objective. With automatic differentiation

*Corresponding author.

E-mail address: wangjingyu@scu.edu.cn (Jingyu Wang)

(AD), PINNs evaluate PDE residuals and optimize network parameters to satisfy the governing equations and boundary conditions. This physics-constrained learning paradigm has shown promise across a range of PDEs, including the Navier-Stokes equations (Rao et al., 2020). To alleviate the ill-conditioned global objectives in standard PINNs, the time-stepping oriented neural network (TSONN) reformulates the optimization in a time-marching manner, embedding classical time-stepping schemes into the learning process (Cao and Zhang, 2025a). Nevertheless, PINNs typically rely on AD (Baydin et al., 2018) in deep-learning frameworks to compute derivatives of the physical fields. When high-order derivatives are required, AD can become prohibitively expensive during backpropagation because it must generate and retain a large number of intermediate tensors (Bhatia and Dangel, 2024) (Gunes Baydin et al., 2015). As a result, PINNs are often difficult to scale to PDEs involving high-order differential operators, since the cost of nested AD grows rapidly with the differentiation order (Baydin et al., 2018) (Bettencourt et al., 2019). Moreover, for complex flows at high Reynolds numbers, PINNs may converge to non-physical pseudo-solutions (Wang et al., 2023).

These limitations have motivated new hybrid approaches that integrate deep learning with classical numerical discretizations, using established schemes to approximate derivatives while retaining the flexibility of learning-based representations (Li et al., 2024) (Lu et al., 2025) (Gao et al., 2022). Training neural networks can be computationally intensive. In addition, when neural networks are embedded within PDE solvers, convergence must be monitored not only through reductions in PDE residuals but also through the optimization of network parameters. This coupling complicates convergence diagnostics and may obscure whether the computed solution has truly converged.

A complementary optimization-based approach is ODIL, which builds on conventional PDE discretizations and does not rely solely on a neural surrogate to represent the solution. Instead, it formulates the governing equations on discretized variables and minimizes a loss constructed from the discretized PDE residuals. The resulting optimization problem can be solved using gradient-based or Newton-type methods. By inheriting the structure and properties of the underlying discretization, ODIL better preserves physical consistency and numerical stability, mitigating ill-conditioned global objectives, unstable gradients, and AD-related overhead that commonly hinder PINNs. In addition, ODIL can be combined with modern machine-learning techniques to accelerate selected numerical components and improve overall computational efficiency. ODIL has been successfully applied to a range of incompressible viscous-flow settings (Karnakov et al., 2023). More recently, the ODIL framework has been extended to jointly infer both obstacle geometry and the associated flow field in three-dimensional steady-state supersonic flows (Buhendwa et al., 2025). In parallel, efforts to improve ODIL efficiency have focused on alleviating loss ill-conditioning: Cao and Zhang (Cao and Zhang, 2025b) proposed the stabilized gradient residual (SGR) loss, which is better conditioned than mean-squared residual objectives and can substantially accelerate convergence.

While ODIL has shown strong performance as an optimization-based PDE solver, existing ODIL formulations have been developed and demonstrated primarily on uniform Cartesian grids, to the best of current knowledge (Karnakov et al., 2024) (Cao and Zhang, 2025b). In practical engineering applications, especially for time-dependent flows with pronounced boundary-layer effects, body-fitted meshes with near-wall refinement are typically essential. Extending discrete optimization-based solvers to such body-fitted geometries therefore remains an important challenge. Beyond geometric considerations, many physical systems evolve in both space and time. In fluid mechanics, these dynamics are governed by the Navier-Stokes equations (Temam, 2024), requiring solvers to accurately capture temporal evolution in addition to spatial structure. Most existing ODIL studies, however, have focused on computing time-invariant solutions or single-time objectives (Karnakov et al., 2024) (Cao and Zhang, 2025b), which limits applicability to convection-dominated flows where the solution undergoes sustained temporal development and complex wake-boundary-layer interactions. These regimes typically demand stable time marching, motivating an ODIL framework that performs trajectory-level optimization over multiple time steps rather than optimizing a single stationary residual. Furthermore, prior ODIL results have been reported mainly on canonical benchmarks such as the lid-driven cavity, where efficiency is typically demonstrated on simple geometries using a single structured grid. The behavior of ODIL on body-fitted multi-block meshes and in more realistic external-flow configurations remains less explored.

Therefore, an ODIL framework that improves geometric adaptability and efficiently addresses flows with time-dependent dynamics is highly desirable. Leveraging the scheme-consistent finite-difference operators in curvilinear coordinates and the multi-block body-fitted treatment introduced in FDGN (Zou et al., 2024), this work enhances the geometric applicability of ODIL and enables discrete-loss optimization on body-fitted multi-block structured meshes. Building on this foundation, a finite-difference-based time-stepping loss optimization solver (FDTO) is developed, which couples ODIL with scheme-consistent finite-difference discretizations and a time-stepping-oriented optimization strategy to improve conditioning, stability, and efficiency while preserving physical consistency. The main contributions are as follows:

- **Geometrically adaptable ODIL on body-fitted grids.** Scheme-consistent finite-difference operators in curvilinear coordinates are integrated into ODIL, enabling discrete-loss optimization directly on body-fitted structured grids (including multi-block configurations). By minimizing discrete residuals with interface-consistent transfers, the resulting formulation improves geometric and boundary-condition compatibility while preserving the efficiency and accuracy of finite-difference discretizations.
- **Time-marching ODIL via trajectory-level optimization.** Time-marching optimization is extended to

the ODIL framework, reformulating the global time-dependent objective into a sequence of time-window sub-problems consistent with the time-marching updates. This ODIL-compatible trajectory decomposition improves conditioning and promotes stable convergence for nonlinear time-dependent optimization.

- **Validation on engineering-relevant configurations.** The proposed method is evaluated on diffusion and nonlinear mixing, as well as incompressible Navier-Stokes cases on body-fitted grids, including the lid-driven cavity, airfoils, and flow around a cylinder. The results demonstrate strong accuracy, robustness, and memory efficiency across geometry-adaptive configurations and long-term temporal evolution.

The remainder of this paper is organized as follows. Section 2 presents the proposed method, including the coordinate-transformed finite-difference discretization and the time-stepping optimization strategy. Section 3 reports results on diffusion equation, flow mixing problem, and incompressible Navier-Stokes equation, and compares proposed method with representative baselines. Finally, Section 4 concludes the paper and discusses limitations and future directions.

2. Methodology

2.1. Paradigms of PDE Solvers

Three representative paradigms for solving PDEs in fluid dynamics are illustrated in Fig. 1: conventional computational fluid dynamics (CFD), FDTO, and PINNs. Although all three target the same governing equations, they differ fundamentally in how PDE constraints are enforced and how the solution is represented and updated.

In conventional CFD solvers, the governing equations are discretized in space and time, and the flow field is advanced through explicit or implicit time-marching schemes. At each time step, large sparse linear or nonlinear systems must be solved, typically involving global matrix assembly and iterative solvers. While this paradigm is well established and numerically robust, its computational cost and memory footprint grow rapidly for fine meshes, complex geometries, and time-dependent simulations, particularly when repeated solves are required in optimization, inverse problems, or parametric studies.

PINNs reformulate PDE solving as a global function-approximation problem, where a neural network is trained to satisfy the governing equations together with boundary conditions, and initial conditions through loss minimization. This mesh-free paradigm avoids explicit matrix assembly and offers strong flexibility for irregular domains. Nevertheless, PINNs introduce new challenges, including high training cost, substantial memory overhead from automatic differentiation, and stiff objectives arising from competing loss terms. These issues become especially pronounced for time-dependent, convection-dominated regimes at high Reynolds numbers, where reliable convergence and accuracy are difficult to guarantee.

The proposed FDTO framework represents a unique intermediate paradigm between classical CFD and PINNs. Similar to CFD, FDTO retains finite-difference discretizations on body-fitted structured grids, thereby preserving the numerical stability, locality, and physical consistency of traditional schemes. In contrast to CFD, FDTO avoids the solution of large algebraic systems. Instead, the discrete flow variables are updated by minimizing a residual-based loss function at each time step, enabling matrix-free updates driven by optimization algorithms.

Compared with PINNs, FDTO optimizes discrete flow variables directly rather than neural-network parameters. This removes the need for network training, reduces the memory overhead of deep automatic-differentiation graphs, and avoids the stiffness associated with global function approximation. By constructing the objective from classical finite-difference operators, FDTO inherits the stability and consistency of established numerical schemes. Moreover, this discrete-optimization viewpoint supports time-marching-oriented optimization for time-dependent problems, while remaining compatible with complex geometries and conventional CFD data structures.

In summary, CFD solves the discretized governing equations, PINNs learn a global neural approximation, and FDTO optimizes discrete flow states. By incorporating coordinate transformations and operates in curvilinear coordinates on body-fitted grids, FDTO improves geometric adaptability for complex geometries. Coupled with finite-difference discretization with time-stepping-oriented optimization, FDTO further achieves a favorable balance among numerical stability, computational efficiency, and modeling flexibility for time-dependent problems.

2.2. FDTO framework

The general formulation of the proposed FDTO framework is shown in Fig. 1. Built on body-fitted structured grids, FDTO casts each time-marching update as a discrete optimization problem, leading to improved conditioning and enhanced numerical stability.

Body-fitted structured grid and node-wise representation: The physical domain is discretized with a body-fitted structured grid a body-fitted structured grid that conforms to the boundary geometry. At each grid node, we store node-wise quantities, including the flow state $\phi = (\mathbf{u}, p)$, precomputed geometric metrics (e.g., $\xi_x, \xi_y, \eta_x, \eta_y, J^{-1}$), and PDE-related parameters. This node-wise representation retains the locality and stencil structure of classical finite-difference schemes, thereby providing a natural basis for discrete optimization over the flow variables.

Curvilinear coordinate transformation: In two dimensions, we consider a coordinate mapping from the physical space (x, y) to the computational space (ξ, η) :

$$\begin{cases} \xi = \xi(x, y) \\ \eta = \eta(x, y) \end{cases} \quad (1)$$

Fig. 2 illustrates a coordinate mapping from the physical domain to the computational domain, where a body-fitted curvilinear grid in the physical space is mapped onto a uniform grid in the computational space. Curves in the same color denote

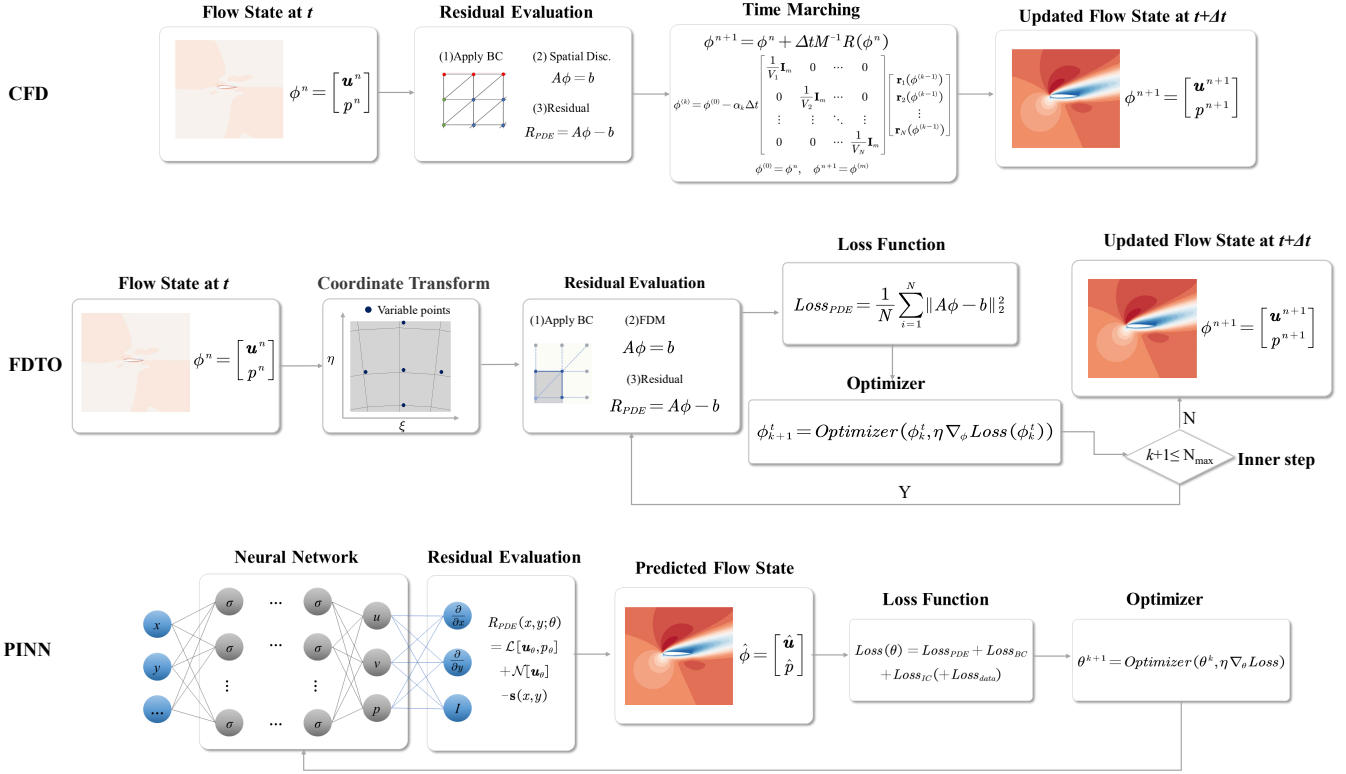


Figure 1: Paradigms of PDE solvers. top: CFD; middle: FDTO; bottom: PINN.

corresponding grid lines (or boundary curves) in the two coordinate systems. Throughout, subscripts denote partial derivatives, for example, $q_x = \partial q / \partial x$. The inverse Jacobian matrix associated with the mapping can be written as

$$J^{-1} = \begin{bmatrix} x_\xi & y_\xi \\ x_\eta & y_\eta \end{bmatrix} = \begin{bmatrix} \xi_x & \eta_x \\ \xi_y & \eta_y \end{bmatrix}^{-1} \quad (2)$$

where the Jacobian determinant is

$$J^{-1} = x_\xi y_\eta - x_\eta y_\xi \quad (3)$$

Accordingly, the metric coefficients (grid derivatives) satisfy:

$$\begin{cases} \tilde{\xi}_x = \xi_x / J = y_\eta \\ \tilde{\xi}_y = \xi_y / J = -x_\eta \\ \tilde{\eta}_x = \eta_x / J = -y_\xi \\ \tilde{\eta}_y = \eta_y / J = x_\xi \end{cases} \quad (4)$$

In practice, the geometric derivatives x_ξ, x_η, y_ξ and y_η are evaluated on the structured grid using finite differences. In this work, these partial-derivative terms are approximated using second-order central finite differences at interior points, while second-order forward and backward finite differences are used near boundaries. The computational mesh spacings are often taken as $\Delta\xi = \Delta\eta = 1$. The coordinate transformation of the PDEs is formulated in a conservative form in computational space. A general two-dimensional conservation-law PDE is

considered in the physical space (x, y) .

$$\frac{\partial Q}{\partial t} + \frac{\partial F}{\partial x} + \frac{\partial G}{\partial y} = 0 \quad (5)$$

where Q is the conserved quantity, and F and G are the fluxes in the x - and y -directions, respectively. Given the coordinate mapping in Eq. (1), physical-space derivatives can be written via the chain rule as

$$\frac{\partial}{\partial x} = \xi_x \frac{\partial}{\partial \xi} + \eta_x \frac{\partial}{\partial \eta}, \quad \frac{\partial}{\partial y} = \xi_y \frac{\partial}{\partial \xi} + \eta_y \frac{\partial}{\partial \eta} \quad (6)$$

Applying Eq. (6) to Eq. (5) results in

$$\frac{\partial Q}{\partial t} + \frac{\partial}{\partial \xi} (\xi_x F + \xi_y G) + \frac{\partial}{\partial \eta} (\eta_x F + \eta_y G) = 0 \quad (7)$$

To retain a conservative form in computational space, the equation is written as

$$\frac{\partial (J^{-1} Q)}{\partial t} + \frac{\partial \tilde{F}}{\partial \xi} + \frac{\partial \tilde{G}}{\partial \eta} = 0 \quad (8)$$

where the transformed (contravariant) fluxes are defined by

$$\tilde{F} = \tilde{\xi}_x F + \tilde{\xi}_y G, \quad \tilde{G} = \tilde{\eta}_x F + \tilde{\eta}_y G \quad (9)$$

Eq. (8) is thus the conservative-form representation of the conservation law in the curvilinear computational coordinates (ξ, η) .

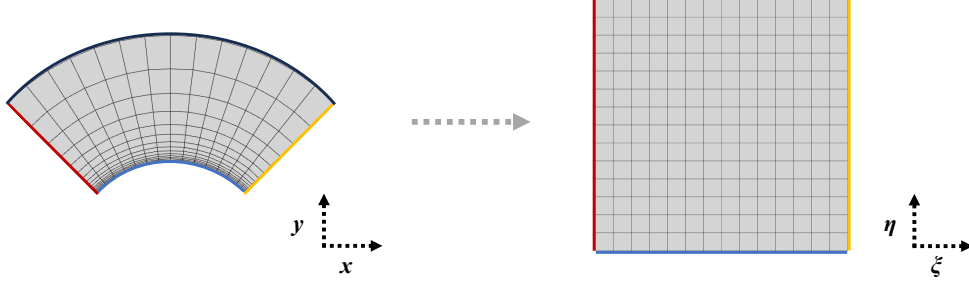


Figure 2: An example of coordinate transformation from physical space (left) to computational space (right).

Boundary Condition: After the coordinate transformation, appropriate boundary closures are applied to ensure a well-posed discrete formulation on body-fitted structured grids. FDTO employs explicit ghost nodes, and boundary treatment is constructed locally using three node sets (Fig. 1): ghost nodes \mathcal{G} outside the physical domain, boundary nodes \mathcal{B} on the physical boundary, and adjacent interior nodes \mathcal{I} involved in near-boundary stencils. For each boundary segment, ghost-node states are populated by a linear extrapolation operator that uses information on \mathcal{B} and \mathcal{I} to maintain stencil consistency for gradient evaluation near the boundary. Specifically, for a generic variable $\phi \in \{\mathbf{u}, p\}$,

$$\phi_{\text{ghost}} = \mathcal{E}_{\text{lin}}(\phi_{\mathcal{B}}, \phi_{\mathcal{I}}) \quad (10)$$

where $\mathcal{E}_{\text{lin}}(\cdot)$ denotes a linear extrapolation along the local boundary-normal direction (equivalently, along the boundary-adjacent grid line). As illustrated by the dashed diagonal in Fig. 1, each boundary node is paired with its nearest interior neighbor along this local normal direction, and the ghost-node value is obtained by linearly extending the same line beyond the boundary. This construction yields a smooth, geometry-consistent closure for near-boundary stencils and provides a unified discrete treatment across different physical boundary specifications without introducing additional penalty terms. Consequently, ghost-node extrapolation preserves locality, maintains consistent residual evaluation near boundaries, and improves robustness during time-stepping optimization.

Finite-difference discretization: Spatial discretization is performed using conservative finite-difference schemes. As illustrated in Fig. 3, interpolation, flux evaluation, and flux divergence are applied at distinct stencil locations, leading to discrete residuals that closely mirror those of classical CFD solvers. Boundary conditions are imposed directly at the discrete level by modifying the residuals associated with boundary nodes, preserving physical constraints without introducing additional penalty terms. Further implementation details of the finite-difference operators and stencil organization please refer to FDGN(Zou et al., 2024). Let n denote the number of nodes of a grid in a d -dimensional space \mathbb{R}^d , the nodal unknowns are stacked as:

$$\phi = [\mathbf{u}_0, p_0, \mathbf{u}_1, p_1, \dots, \mathbf{u}_{n-1}, p_{n-1}]^T \in \mathbb{R}^{3n} \quad (11)$$

where $\mathbf{u}_j = [u_j, v_j]^T$ and p_j denote the velocity vector and pressure at node $j \in n$, respectively. A class of nonlinear PDEs is

considered in the form:

$$\mathcal{N}[\phi](x, y, t) = f_s(x, y, t) \quad (x, y) \in \Omega, t \in \Gamma \quad (12)$$

where \mathcal{N} denotes a nonlinear differential operator, $\phi(x, y)$ is the unknown solution field, and $f_s(x, y)$ is the source term. The physical domain Ω is discretized and \mathcal{N} is approximated by finite differences scheme, yielding a system of nonlinear algebraic equations that can be written compactly as a discrete residual:

$$\mathbf{r}_{\text{PDE}}(\phi) = 0 \quad (13)$$

Residual-based loss formulation: A locally linearized residual system is considered, given by:

$$f = \mathbf{A}\phi - \mathbf{b} = 0 \quad (14)$$

where $\mathbf{A} \in \mathbb{R}^{n \times n}$ is the Jacobian matrix (or linearized residual operator), $\phi \in \mathbb{R}^n$ is the discretized solution vector, and $\mathbf{b} \in \mathbb{R}^n$ is the source term evaluated at the current iterate ϕ^k , with k representing the time step.

The finite-difference discretization leads to the residual system

$$\mathbf{r}_{\text{PDE}}(\phi) = \mathbf{A}\phi - \mathbf{b} \quad (15)$$

which is incorporated into the loss function

$$\mathcal{L}_{\text{PDE}}(\phi) = \frac{1}{N} \sum_{i=1}^N \|r_{\text{PDE},i}(\phi)\|^2 \quad (16)$$

This approach avoids the need for global matrix inversion, while maintaining the numerical consistency of the underlying discretization scheme.

The FDTO minimizes the loss function using gradient-based optimizers, such as Adam (Kingma, 2014), Soap (Vyas et al., 2024), or L-BFGS (Zhu et al., 1997). The full loss function is given by

$$\mathcal{L}_{\text{PDE}}(\phi) = \frac{1}{N} \sum_{i=1}^N \|A\phi - b\|_2^2 \quad (17)$$

2.3. Time-stepping Method

For a time-dependent PDE written in semi-discrete form:

$$\frac{\partial \phi}{\partial t} + \mathcal{N}(\phi) = 0 \quad (18)$$

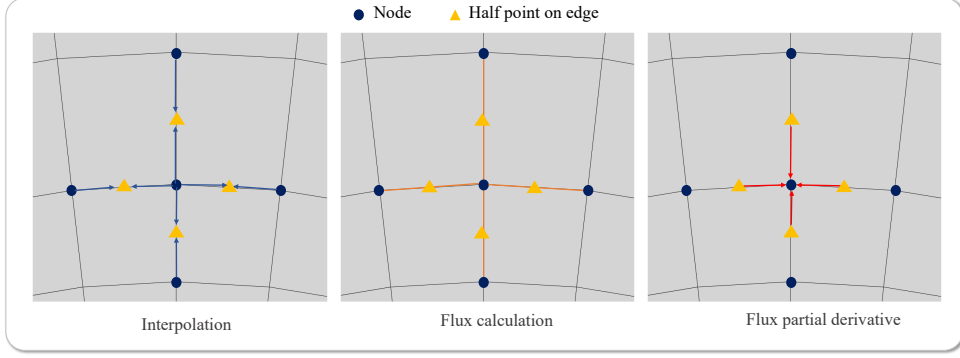


Figure 3: Diagram of FDTO spatial discretization procedure. (left) Node-stored variables (and precomputed grid metrics) are linearly interpolated to edge midpoints to obtain face states. (middle) Conservative numerical fluxes are evaluated on these faces using the interpolated states. (right) The nodal residual is assembled by a finite-difference flux divergence, i.e., differences of neighboring face fluxes in the computational ξ/η directions.

the discrete state ϕ^n is advanced to ϕ^{n+1} using the unified scheme:

$$\frac{\phi^{n+1} - \phi^n}{\Delta t} + \alpha \mathcal{N}(\phi^n) + (1 - \alpha) \mathcal{N}(\phi^{n+1}) = 0 \quad \alpha \in \{0, 0.5, 1\} \quad (19)$$

where Δt is the time-step size and $\mathcal{N}(\cdot)$ denotes the spatial operator after finite-difference discretization (including boundary treatments). The parameter α controls the degree of implicitness: $\alpha = 1$ recovers the forward (explicit) Euler scheme, $\alpha = 0$ corresponds to the backward (implicit) Euler scheme, and $\alpha = 0.5$ yields the Crank-Nicolson discretization (Crank and Nicolson, 1947).

Instead of advancing Eq. (19) with a conventional time-integration implementation (e.g., explicit marching, or implicit updates requiring the solution of linear/nonlinear systems at each step), FDTO treats ϕ^{n+1} as the optimization variable and minimizes the norm of the discrete residual at each time step. A local-in-time optimization subproblem is formulated and solved, initialized from ϕ^n :

$$\phi^{n+1} = \arg \min_{\phi} \mathcal{L}_{\text{PDE}}^{n+1}(\phi; \phi^n) \quad (20)$$

This time-marching optimization enhances conditioning by restricting each optimization solve to a single time-step update, rather than optimizing over the entire time horizon at once. In addition, the finite-difference discretization provides residual scaling/normalization, which keeps the gradients well balanced across state components (e.g., velocity and pressure) and thereby promotes stable convergence under first-order/quasi-Newton optimizers.

Within each time step, the optimizer iteratively updates the candidate state via

$$\phi^{n+1} \leftarrow \text{Optimizer}(\phi^{n+1}, \eta \nabla_{\phi^{n+1}} \mathcal{L}_{\text{PDE}}^{n+1}) \quad (21)$$

where η is the learning rate and the gradient is taken with respect to ϕ^{n+1} . At the end of inner loop, the optimized state $\phi^{n+1} = (\mathbf{u}^{n+1}, p^{n+1})$ is accepted and used to initialize the next step, thereby continuing the time-marching process.

2.4. Optimization Algorithm

Algorithm 1 summarizes the procedure for advancing the solution within the FDTO framework and serves as the basis for the algorithmic workflow discussed in this subsection.

The current solution ϕ_k serves as the initialization for the inner iterations, during which discrete residuals are evaluated and minimized. All spatial operators are applied locally through a finite-difference operator \mathcal{N} , while boundary conditions are enforced to residual evaluation to ensure valid stencil access near domain boundaries.

Mesh-related quantities, including coordinate metrics and connectivity information, are precomputed and remain fixed throughout the optimization. As a result, each inner iteration operates only on the evolving flow variables, enabling efficient and stable loss and gradient evaluations. The optimization terminates when the maximum number of inner iterations is reached.

Once the inner-loop optimization terminates, the updated state is accepted as ϕ^{n+1} and the algorithm proceeds to the next time step. The optimizer state is reset before each new step to avoid carrying over step-specific history. This local-in-time strategy circumvents global matrix assembly and inversion, while preserving the stencil structure and numerical stability of the underlying finite-difference discretization.

Furthermore, an additional stabilization strategy is introduced to mitigate error accumulation and suppress pressure oscillations in wake-dominated airfoil flows. As illustrated in Fig. 4, a node-to-cell-to-node (N-C-N) averaging operator is applied as a local smoothing on body-fitted structured meshes. First, cell-centered values are computed as the arithmetic mean of the four corner nodal values for each adjacent cell. Next, these cell-center values are pairwise averaged along the computational ξ direction to obtain two intermediate face-centered values. Finally, the two face-centered values are averaged along the η direction to update the nodal value. This purely discrete, locality-preserving procedure damps high-frequency numerical noise that may accumulate during optimization-driven time marching, thereby improving the stability of pressure reconstruction in regions with strong shear and sharp gradients. In practice, the N-C-N smoothing is applied after each outer time-

Algorithm 1: Finite difference and time-stepping optimization

Require: $[\mathbf{u}_0, p_0]$; time step Δt ; learning rate η ; max steps K_{\max} ;

Ensure: Optimized ϕ ; trajectory $[\phi_k]_{k=0}^{K_{\max}}$

1 **Initialize:** $\phi \leftarrow [\mathbf{u}_0, p_0]$; Precomputed mesh metrics $[\xi_x, \eta_x, \xi_y, \eta_y, J^{-1}]$

2 **Define:** FDM operator \mathcal{N} ; Optimizer

3 **while** not reached max steps ($k < K_{\max}$) **do**

4 **for** $i \leftarrow 0$ to $N_{\text{inner}} - 1$ **do**

5 $\phi^*|_{\partial\Omega} \leftarrow \text{ImposeBC}(\phi)$

6 $\phi_k^i \leftarrow \mathcal{N}(\phi^*)$

7 $\mathcal{L}_{\text{PDE}}(\phi) \leftarrow \frac{1}{N} \sum_{i=1}^N \|\mathcal{r}_{\text{PDE},i}(\phi_k^i)\|^2$

8 $i \leftarrow i + 1$

9 $\phi_k^{i+1} \leftarrow \text{Optimizer}(\phi_k^i, \nabla \mathcal{L}_{\text{PDE}}(\phi), \eta)$

10 $k \leftarrow k + 1$

11 $\phi_{k+1} \leftarrow \phi_k^{N_{\text{inner}}-1}$

12 Reset Optimizer

13 **return** ϕ_K

marching update to enhance interface consistency and suppress spurious oscillations on curvilinear body-fitted meshes.

3. Results and Discussions

This section assesses the proposed FDTO solver on a set of representative cases spanning different mesh configurations, boundary conditions, and physical models, with primary emphasis on incompressible Navier-Stokes equations. The incompressible tests include lid-driven cavity benchmarks, external airfoil aerodynamics on body-fitted grids, and a cylinder case on a multi-block structured mesh. Since ODIL baselines are not yet available for time-dependent PDEs in the current setting, the diffusion equation and a nonlinear flow-mixing problem are included as additional evaluations to demonstrate broader applicability. Reference solutions are taken from analytical expressions when available, and otherwise obtained from a conventional CFD solver (e.g., COMSOL). The relative L_2 error, defined as $\|\phi_{\text{opt}} - \phi_{\text{ref}}\|_{L_2} / \|\phi_{\text{ref}}\|_{L_2}$ is used for all subsequent error calculations. Here, ϕ_{opt} denotes the optimized solution obtained from the proposed method. The reference solution ϕ_{ref} represents the ground-truth solution used for comparison. All experiments are conducted on an NVIDIA GeForce RTX 5090. The implementation of the FDTO solver is publicly available at <https://github.com/My-git96/FDTPDE>.

Tab. 1 summarizes the case configurations used to validate the proposed solver. The test set includes incompressible Navier-Stokes cases covering both internal and external flows (lid-driven cavity, airfoil, and cylinder), together with diffusion and nonlinear flow mixing problem on a square domain. Three mesh types are considered: a uniform Cartesian grid for the square and cavity cases, a curvilinear body-fitted grid for the airfoil configuration, and a multi-block mesh for the cylinder

case. L-BFGS is used for the uniform-grid problems, whereas the airfoil and cylinder cases adopt the SOAP optimizer with a smaller learning rate. The time-step size Δt , epoch budget, and inner-iteration count are selected case by case to reflect differences in conditioning and geometric complexity, enabling a systematic assessment of robustness and accuracy across physical models, geometries, and mesh configurations.

3.1. Lid-driven Cavity

To begin the incompressible Navier-Stokes evaluation with a well-established internal-flow benchmark, the lid-driven cavity flow is considered. This canonical test enables a clear assessment of numerical accuracy, and high-fidelity reference data are available (Ghia et al., 1982). The physical domain is the unit square $[0, 1] \times [0, 1]$ and is discretized on a structured 201×201 grid. As shown in Fig. 5, no-slip velocity conditions are imposed on the stationary walls, while the top lid moves with a prescribed tangential velocity $(u, v) = (1, 0)$. For pressure, a homogeneous Neumann condition $\partial p / \partial n = 0$ is applied on all boundaries. The performance of FDTO is compared with ODIL-SGR (Cao and Zhang, 2025b) and representative PINN-based neural discretization (PINN-ND) solvers (Zou et al., 2024) (Li et al., 2025).

Fig. 6 illustrates the predicted velocity fields and the corresponding error maps at $\text{Re} = 2500$ and $\text{Re} = 5000$. ODIL-SGR achieves errors comparable to (and slightly lower than) FDTO at $\text{Re} = 2500$, but its accuracy degrades markedly at $\text{Re} = 5000$, where the errors become substantially larger than FDTO. By contrast, FDTO maintains consistently low error levels at both Reynolds numbers, indicating improved robustness as convection effects intensify with increasing Re . The streamline visualizations in Fig. 7 further corroborate the field-level comparison. FDTO reliably reproduces the expected vortex topology from $\text{Re} = 2500$ to $\text{Re} = 7500$, including the emergence of the characteristic multi-vortex structure at higher Reynolds numbers.

To probe a more challenging regime, the $\text{Re} = 10000$ case is initialized from the converged solution at $\text{Re} = 3200$. Time marching is then performed with $\Delta t = 0.05$. Fig. 8 shows instantaneous streamlines at representative time instances, illustrating the temporal evolution of the vortex structures.

Beyond qualitative visualization, Fig. 9 reports representative centerline profiles, including velocity and pressure distributions along the cavity centerlines. These profiles provide a concise quantitative check of the flow structure, and confirm that FDTO reproduces the expected near-wall behavior and overall recirculation patterns in the time-dependent case. Fig. 10 summarizes the convergence histories. Across Reynolds numbers, FDTO exhibits faster error reduction and consistently lower relative L_2 errors than ODIL-SGR, with the performance gap widening as Re increases and the optimization landscape becomes more nonlinear. Consistent with these trends, Tab. 2 reports the minimum achieved error and the corresponding runtime, highlighting the efficiency advantage of FDTO at higher Reynolds numbers. Notably, at $\text{Re} = 7500$, ODIL-SGR fails to converge to a stable solution, whereas FDTO still reaches a low-error state within a finite runtime.

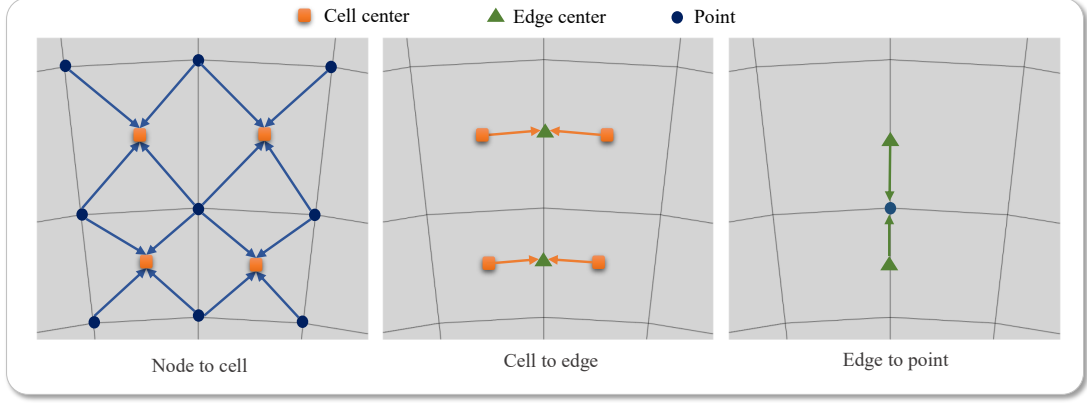


Figure 4: Schematic of N-C-N averaging operator on body-fitted meshes.

Table 1: Case configurations for evaluating the FDTO solver.

Equation Type	Geometry	Mesh type	Mesh size	Optimizer	Epoch	Delta t	Inner-iteration	Learning rate
Diffusion	Square	Uniform	101*101	L-BFGS	100	1/100	100	1.0
Flow Mixing	Square	Uniform	256*256	L-BFGS	256	1/64	100	1.0
Incompressible Navier-Stokes	Lid-driven Cavity	Uniform	201*201	L-BFGS	1000	1/10	100	1.0
	Airfoil	Curvilinear	399*150	Soap	1000	1/100	2000	5e-4
	Cylinder	Multi-block	29801	Soap	3000	1/10	2000	5e-4

Table 2: Comparison of minimum error and convergence time for FDTO and ODIL-SGR in lid-driven cavity flow(201 × 201).

Method	Re = 2500		Re = 3200		Re = 5000		Re = 7500	
	relative L_2 error	t (s)						
FDTO	0.05	1193	0.05	1409	0.06	2291	0.12	4510
ODIL-SGR	0.05	1689	0.06	2452	0.20	2445	0.57	-

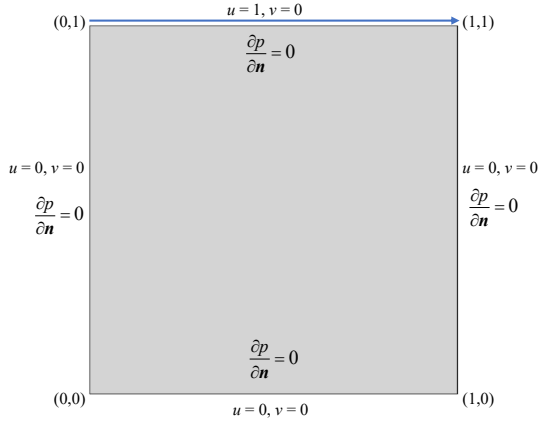


Figure 5: Boundary Conditions for the lid-driven cavity (Uniform).

Finally, FDTO is compared with representative PINN-ND solvers by assessing practical efficiency (per-epoch runtime and GPU memory usage) together with convergence stability. The convergence curves in Fig. 11 highlight the stability of the proposed framework: FDTO exhibits smooth, nearly monotonic error decay, whereas FDGN and Gen-FVGN converge more slowly and show more pronounced oscillations, suggesting reduced optimization stability. From an efficiency stand-

point, Tab. 3 further shows that FDTO achieves a substantially smaller GPU memory footprint than Gen-FVGN while maintaining competitive runtime, indicating a favorable trade-off between memory usage and computational speed. This trend is consistent with the core design of FDTO, where the unknown fields are optimized directly on discrete degrees of freedom under physics constraints rather than being represented by a global neural parameterization. By avoiding backpropagation through deep network surrogates and their associated intermediate activations, FDTO reduces memory overhead and maintains stable coupled updates of velocity and pressure under challenging dynamics.

Table 3: Comparison of GPU memory usage and time costs per epoch for different methods in lid-driven cavity flow(201 × 201, Re = 2500).

Method	GPU memory (MB)	Time cost per epoch (s)
FDGN	4072	2.52
Gen-FVGN	7611	2.22
FDTO	710	1.02

3.2. AirFoil Flow

When extending the evaluation from canonical internal flows to external aerodynamic configurations, pressure reconstruction

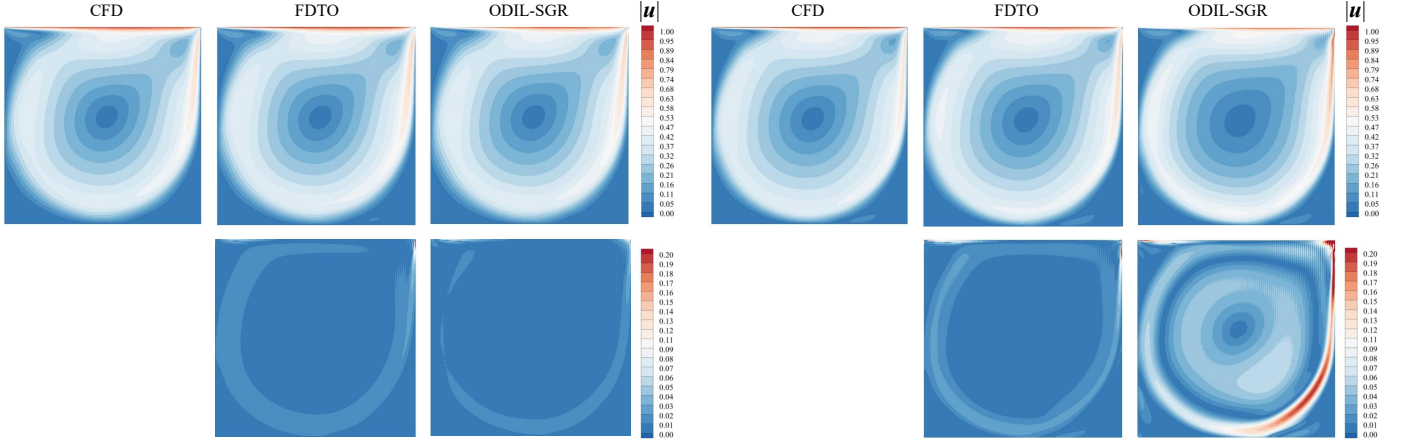


Figure 6: Comparison of CFD, FDTO, and ODIL-SGR for the lid-driven cavity at $Re = 2500$ (left) and $Re = 5000$ (right), showing velocity fields and absolute error maps on a 201×201 grid.

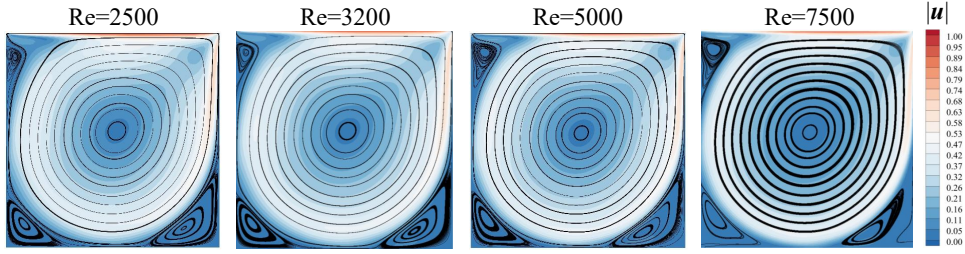


Figure 7: FDTO-optimized streamlines for lid-driven cavity flow from $Re = 2500$ to $Re = 7500$ on a 201×201 grid.

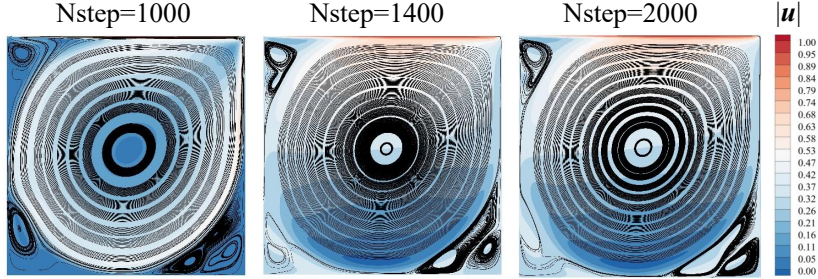


Figure 8: FDTO-optimized lid-driven cavity streamlines at $Re = 10000$ on a 201×201 grid for different time steps ($N_{\text{step}} = 1000, 1400, 2000$).

becomes more challenging on body-fitted grids, especially in wake-dominated regions where strong shear and sharp gradients may trigger oscillations during optimization-based time stepping. This subsection focuses on engineering-relevant airfoil cases. The goal is to assess geometric adaptability on body-fitted structured grids, robustness of pressure reconstruction in convection-dominated regimes, and preservation of key aerodynamic quantities of interest. Four representative airfoils (NACA0012, NACA4424, RAE2822, and RAE5214) are considered, as shown in Fig. 12 and summarized in Tab. 4. Unless otherwise specified, all cases are computed on a 399×150 body-fitted structured grid (Fig. 13). The computational domain consists of an upstream semicircular far-field boundary and the top/bottom far-field boundaries, together with a down-

stream outlet boundary, the airfoil surface is treated as a solid wall. On the far-field boundary, a uniform free stream with angle of attack α is prescribed for velocity, while a homogeneous Neumann condition is imposed for pressure: $(u, v) = (\cos \alpha, \sin \alpha)$, $\partial p / \partial n = 0$, where n denotes the outward unit normal. On the outlet boundary, a reference pressure is prescribed and zero-normal-gradient conditions are applied to the velocity: $p = 0$, $\partial u / \partial n = 0$ and $\partial v / \partial n = 0$. On the airfoil wall, a no-slip condition is imposed: $u = 0$ and $v = 0$. All boundary specifications are enforced through the ghost-node linear extrapolation closure described in Sec. 2.2, ensuring stencil-consistent gradient evaluation near the body-fitted boundary and stable pressure reconstruction in the wake region.

Fig. 14 visualizes the velocity and pressure fields for the air-

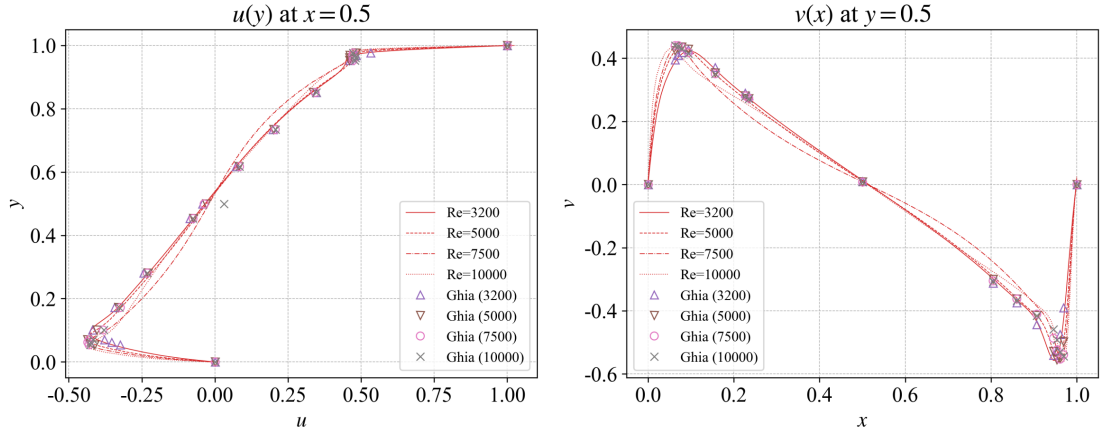


Figure 9: Comparisons of horizontal velocity along the vertical centerline (left) and vertical velocity along the horizontal centerline (right) for the time-averaged lid-driven cavity flows at $Re = 2500$ on a 201×201 grid.

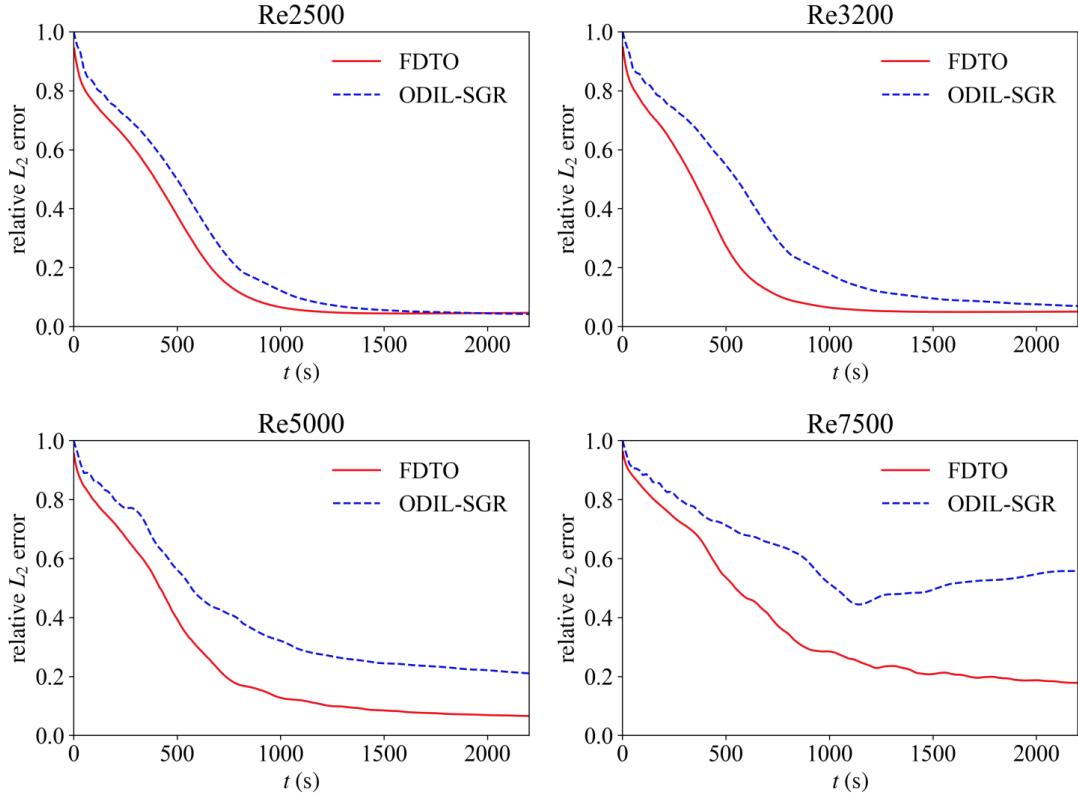


Figure 10: Convergence comparison of FDTO and ODIL-SGR for lid-driven cavity flow on a 201×201 grid: relative L_2 error versus runtime at $Re = 2500, 3200, 5000,$ and 7500 .

Table 4: Airfoil test-case configurations (Reynolds number and angle of attack).

Cases	Re	α
NACA0012	100	15°
NACA4424	200	11°
RAE2822	500	7°
RAE5214	1000	3°

foil cases, comparing the reference CFD solutions with the predictions of FDTO and the parametric solver (Cao et al., 2025). For each case, velocity-magnitude contours and absolute velocity errors are reported, together with pressure contours and absolute pressure errors. Across all configurations, FDTO reproduces the global flow topology around the airfoil and yields small errors that remain mainly localized to sharp-gradient regions (e.g., near the trailing edge and the near wake), supporting geometric adaptability and flow field fidelity on body-fitted grids. By comparison, the parametric solver exhibits larger

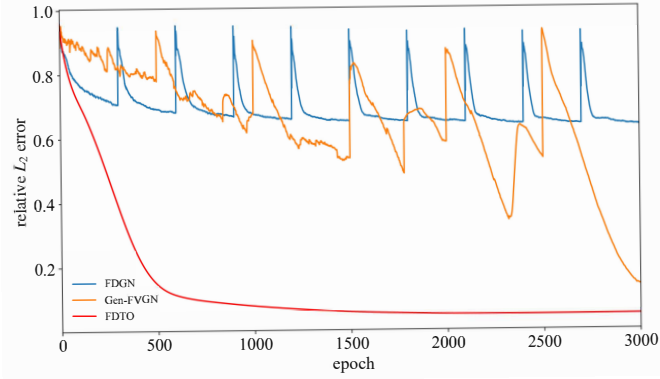


Figure 11: Convergence comparison on lid-driven cavity flow at $Re = 2500$ on a 201×201 grid: relative L_2 error versus epoch for FDTO, FDGN, and Gen-FVGN.

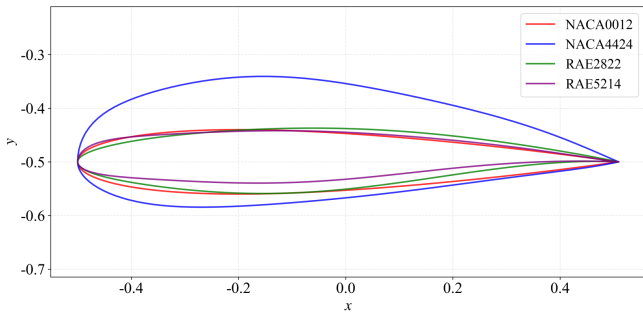


Figure 12: Representative airfoil geometries (NACA0012, NACA4424, RAE2822, and RAE5214).

and more spatially distributed errors, particularly in the downstream wake, indicating reduced robustness in shear-dominated regions.

Beyond flow-field contours, wall-pressure consistency is assessed using the surface pressure distribution, a sensitive diagnostic for external aerodynamics. Fig. 15 shows that FDTO closely matches the CFD reference across all airfoils, capturing both the leading-edge suction peak and the downstream pressure recovery for symmetric and cambered geometries. By contrast, the parametric solver exhibits more pronounced deviations near strong-gradient regions, consistent with the error patterns observed in the wake and trailing-edge vicinity.

Following the qualitative field comparisons in Fig. 14, quantitative assessments are further reported in terms of solution errors and integrated aerodynamic loads. Tab. 5 reports the relative L_2 errors of $|\mathbf{u}|$ and p across all cases. FDTO attains consistently lower velocity errors while maintaining competitive pressure accuracy, with more pronounced gains in configurations featuring stronger nonlinear wake interactions (e.g., RAE2822). Beyond field-level metrics, Tab. 6 compares the lift and drag coefficients among CFD, the parametric solver, and FDTO. Across different Reynolds numbers and angles of attack, FDTO remains in close agreement with the CFD references and exhibits reduced deviations—particularly in drag for the more nonlinear cases—indicating that improved flow and pressure reconstruction translates into reliable integrated aero-

dynamic loads.

3.3. Cylinder

To assess geometric adaptability on multi-block structured grids, incompressible flow around a cylinder in a channel is considered. In this setting, block interfaces and inter-block connectivity may introduce numerical artifacts unless the discrete state remains coherent across blocks. As shown in Fig. 16, the computational domain is a rectangle $(x, y) \in [0, 2.2] \times [0, 0.41]$ with a circular cylinder embedded near the inlet. The mesh is partitioned into multiple structured blocks. A body-fitted, locally refined block surrounds the cylinder to resolve near-wall gradients and separated shear layers, while an elongated downstream block uses stretched spacing to efficiently capture wake development. The resulting multi-block mesh contains approximately 2.98×10^4 points, together with connectors associated with block interfaces. The left boundary is prescribed as a uniform inflow: $u = u_{in}$, $v = 0$, $\partial p / \partial n = 0$. On the cylinder surface and the channel walls (top and bottom), no-slip conditions are enforced: $u = 0$, $v = 0$, $\partial p / \partial n = 0$, where n denotes the outward unit normal. At the right boundary, a reference pressure is prescribed as $p = 0$, and a compatible outflow pressure closure is applied via ghost-node extrapolation consistent with the near-boundary stencils. All boundary conditions and inter-block interface continuity are enforced using the unified ghost-node linear extrapolation and interface-consistent transfer operators described in Sec. 2.2, helping maintain cross-block coherence and suppress spurious oscillations near block connectors.

With the multi-block mesh and boundary conditions specified above, solution quality and cross-block coherence are assessed on this external-flow case. Fig. 17 compares the CFD reference solution with FDTO for the velocity magnitude $|\mathbf{u}|$ and pressure p , along with the corresponding absolute error maps. FDTO reproduces the dominant wake physics, including acceleration/deceleration around the cylinder, the low-speed recirculation region, and the downstream evolution of separated shear layers. Quantitatively, FDTO attains relative L_2 errors of 4.1651×10^{-2} for $|\mathbf{u}|$ and 6.7093×10^{-2} for p , demonstrating agreement with the CFD reference in both velocity and pressure fields. Importantly, the errors remain localized to gradient-dominated regions (e.g., near-wall pressure variations and the shear-layer/wake core) rather than forming bands aligned with block interfaces. This indicates that the proposed framework preserves cross-block field coherence and mitigates interface-related artifacts on multi-block grids.

3.4. Diffusion Equation

Accordingly, a nonlinear diffusion equation is considered as a representative parabolic PDE widely used to describe heat and scalar transport processes (Cho et al., 2023). The governing equation is given by

$$\partial_t u = \alpha (\|\nabla u\|^2 + u \Delta u), \quad x \in \Omega, \quad t \in \Gamma \quad (22)$$

subject to the initial and boundary conditions

$$u(x, 0) = u_{ic}(x), \quad x \in \Omega \quad (23)$$

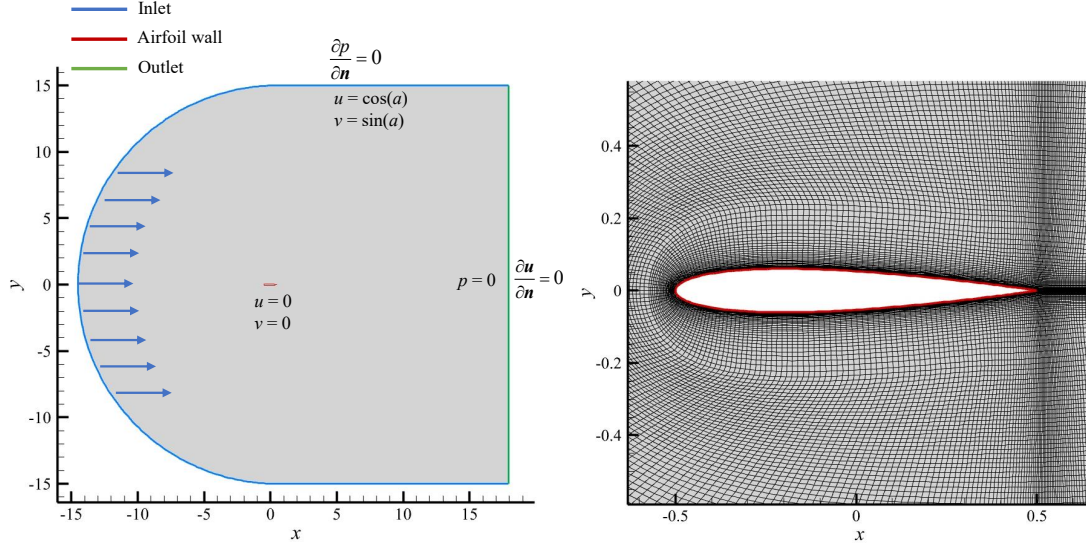


Figure 13: Computational domain, boundary conditions (left), and body-fitted structured mesh (right) for airfoil flows (curvilinear).

Table 5: Relative L_2 errors of $|\mathbf{u}|$ and p for airfoil cases: FDTO versus the parametric solver.

Cases	Method	$ \mathbf{u} $ Relative L_2 Error	p Relative L_2 Error
NACA0012 (Re = 100, $\alpha = 15^\circ$)	ParametricSolver	0.016	0.060
	FDTO	0.011	0.068
NACA4424 (Re = 200, $\alpha = 11^\circ$)	ParametricSolver	0.016	0.049
	FDTO	0.012	0.069
RAE2822 (Re = 500, $\alpha = 7^\circ$)	ParametricSolver	0.014	0.054
	FDTO	0.009	0.033
RAE5214 (Re = 1000, $\alpha = 3^\circ$)	ParametricSolver	0.009	0.042
	FDTO	0.008	0.049

Table 6: Comparison of lift and drag coefficients (C_l , C_d) for airfoil cases: CFD, FDTO, and the parametric solver.

Cases	Method	C_l	C_d
NACA0012(Re = 100, $\alpha = 15^\circ$)	CFD	0.6626	0.5036
	ParametricSolver	0.6727	0.4826
	FDTO	0.6498	0.5118
NACA4424 (Re = 200, $\alpha = 11^\circ$)	CFD	0.3223	0.3821
	ParametricSolver	0.3498	0.3770
	FDTO	0.3391	0.3947
RAE2822 (Re = 500, $\alpha = 7^\circ$)	CFD	0.3581	0.1849
	ParametricSolver	0.3741	0.1833
	FDTO	0.3742	0.1889
RAE5214 (Re = 1000, $\alpha = 3^\circ$)	CFD	0.2191	0.1176
	ParametricSolver	0.2222	0.1187
	FDTO	0.2244	0.1203

$$u(x, t) = 0, \quad t \in \Gamma \quad (24)$$

tion of three Gaussian functions:

$$u_{ic}(x, y) = 0.25 \exp[-10\{(x - 0.2)^2 + (y - 0.3)^2\}] + 0.4 \exp[-15\{(x + 0.1)^2 + (y + 0.5)^2\}] + 0.3 \exp[-20\{(x + 0.5)^2 + y^2\}] \quad (25)$$

The spatial domain is defined as $\Omega = [-1, 1]^2$, and the temporal domain is $\Gamma = [0, 1]$. The diffusion coefficient is set to $\alpha = 0.05$. The initial condition is constructed as a superposi-

A comparative study is conducted between the proposed FDTO solver, separable PINN (SPINN), and a standard PINN,

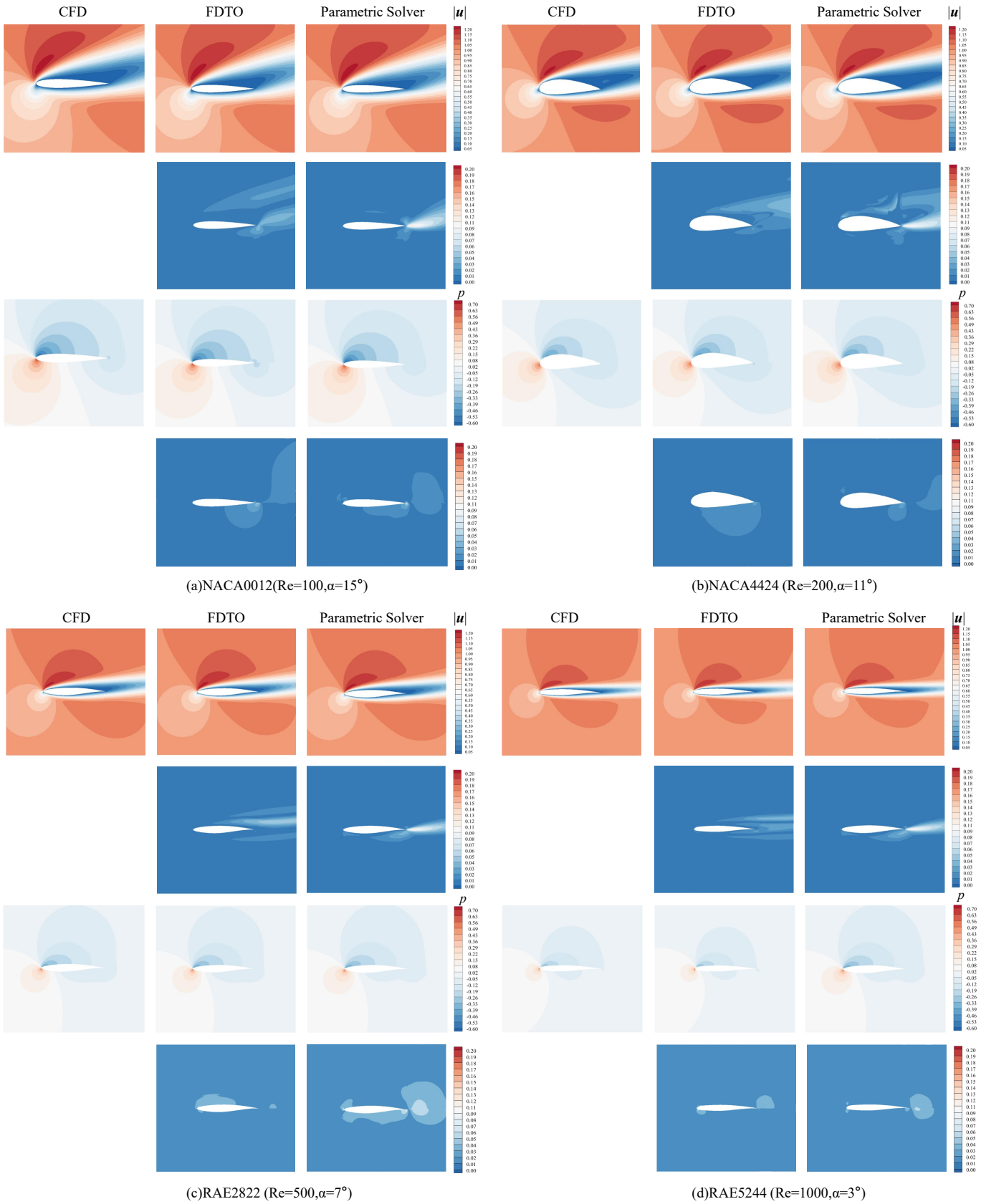


Figure 14: Comparison of airfoil flow fields and absolute error maps. For each case, the columns (left to right) show the reference CFD solution, FDTO prediction, and the parametric solver prediction. The rows (top to bottom) report the velocity-magnitude contours, the absolute velocity error, the pressure contours, and the absolute pressure error.

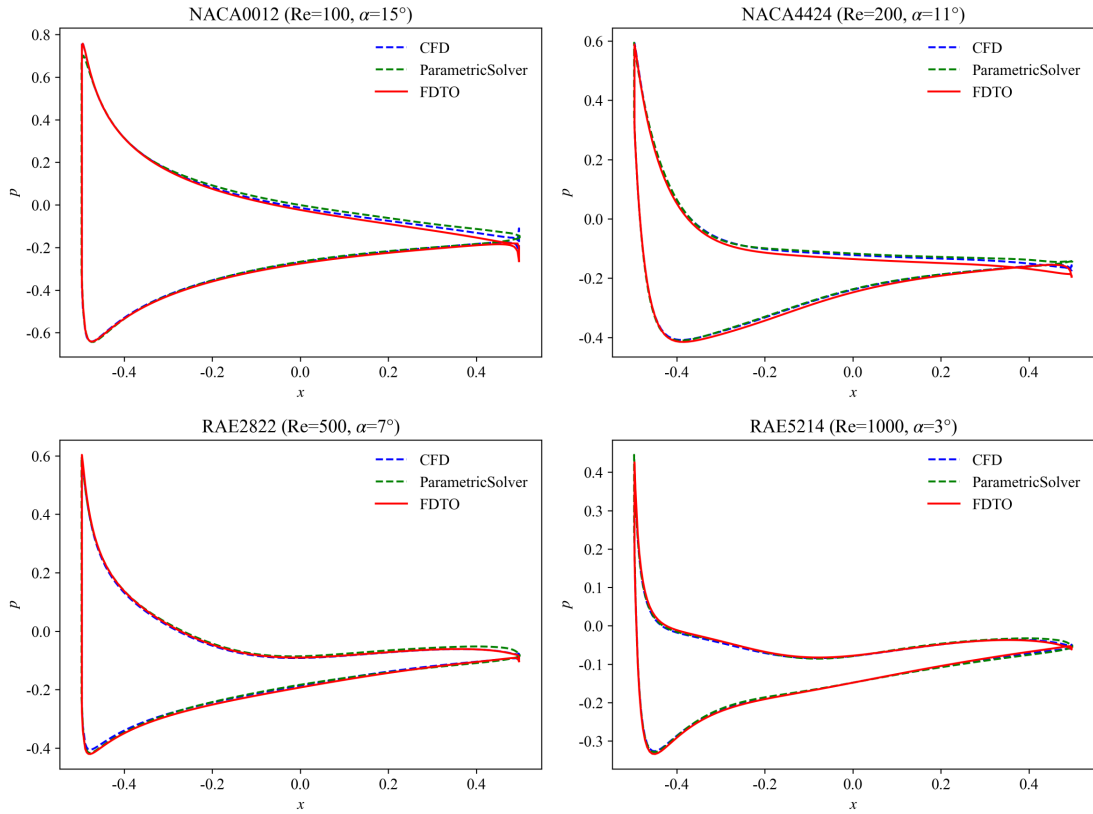


Figure 15: Comparison of surface pressure distributions: CFD, FDTO, and the parametric solver. Top-left: NACA0012(Re = 100, $\alpha = 15^\circ$); top-right: NACA4424(Re = 200, $\alpha = 11^\circ$); bottom-left: RAE2822(Re = 500, $\alpha = 7^\circ$); bottom-right: RAE5214(Re = 1000, $\alpha = 3^\circ$).

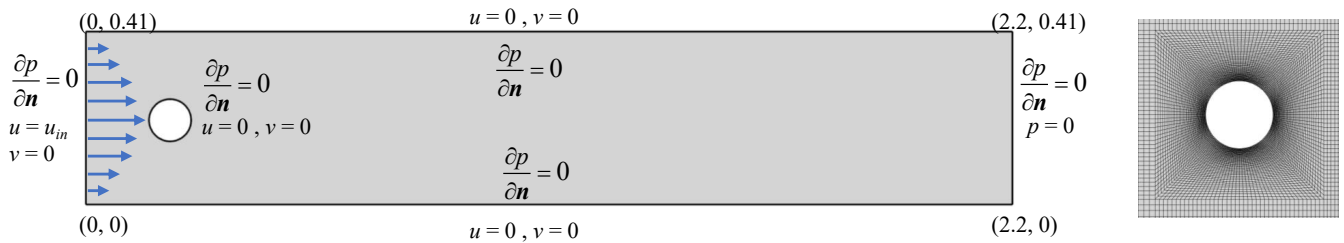


Figure 16: Cylinder-in-channel configuration: boundary conditions (left) and the body-fitted multi-block structured mesh (right).

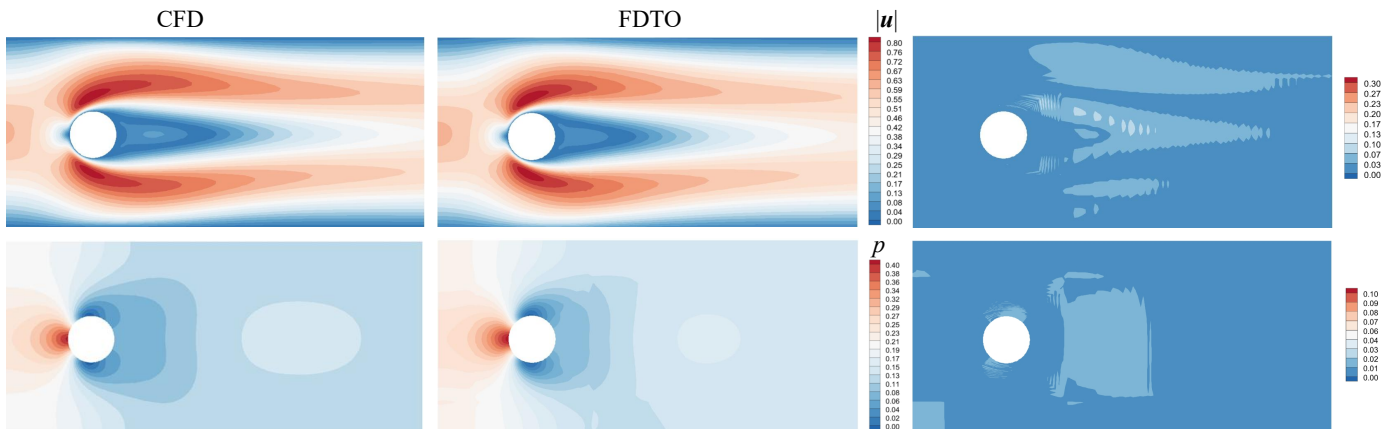


Figure 17: Comparison of FDTO against CFD for cylinder flow. Top row: velocity-magnitude and error; bottom row: pressure fields and error.

using the reference solution reported in (Cho et al., 2023) as the ground-truth baseline. Fig. 18 presents the solution fields together with the corresponding absolute error maps on a 101×101 grid at $t = 0, 0.5$, and 1. Both FDTO and SPINN closely reproduce the reference solution across all snapshots, with small errors that remain confined to localized regions. In contrast, the standard PINN exhibits noticeable deviations in the background region and near steep gradients, together with spatially diffuse error patterns. Consistent with these distributions, the PINN yields substantially larger errors at all time instances, indicating reduced fidelity in capturing the diffusion dynamics under the same evaluation setting. These results suggest that optimizing directly over discrete degrees of freedom allows FDTO to preserve diffusion dynamics with localized, physically consistent errors, while avoiding the diffuse error spread characteristic of a globally parameterized PINN.

Consistent with the trends observed in the solution and error contours, Tab. 7 provides a quantitative comparison of relative L_2 error and GPU memory consumption for the diffusion equation. FDTO maintains low errors at $t = 0, 0.5$, and 1, while SPINN achieves comparable (slightly smaller) errors. From a computational perspective, SPINN is the most memory-efficient, requiring 590 MB of GPU memory. FDTO uses slightly more memory (636 MB) but remains lightweight and practical. In contrast, the PINN requires 8762 MB—over an order of magnitude higher than both FDTO and SPINN (approximately 13.8 times compared with FDTO). Taken together, these results indicate that FDTO achieves near-SPINN-level accuracy while maintaining low GPU memory usage, and substantially outperforms the PINN baseline in both accuracy and memory footprint on this diffusion test.

Table 7: Comparison of relative L_2 error and GPU memory for the diffusion equation on a 101×101 grid.

Method	relative L_2 error			GPU memory (MB)
	$t = 0$ s	$t = 0.5$ s	$t = 1$ s	
SPINN	0.005	0.004	0.003	590
PINN	0.046	0.034	0.038	8762
FDTO	0.004	0.005	0.005	636

3.5. Flow Mixing Problem

To further assess the proposed solver, a more challenging nonlinear (2 + 1)-dimensional mixing-flow case is considered, representing the mixing of two fluids. Following the setup in CAN-PINNs (Cho et al., 2023)(Chiu et al., 2022), the governing equation is given by

$$\frac{\partial u(t, x, y)}{\partial t} + a \frac{\partial u(t, x, y)}{\partial x} + b \frac{\partial u(t, x, y)}{\partial y} = 0, \quad (26)$$

$$t \in [0, 4], \quad x \in [-4, 4], \quad y \in [-4, 4]$$

where

$$a(x, y) = -\frac{v_t}{v_{t,\max}} \frac{y}{r} \quad (27)$$

$$b(x, y) = \frac{v_t}{v_{t,\max}} \frac{x}{r} \quad (28)$$

$$v_t = \operatorname{sech}^2(r) \tanh(r) \quad (29)$$

$$r = \sqrt{x^2 + y^2} \quad (30)$$

with $v_{t,\max} = 0.385$. The spatial domain is $\Omega = [-4, 4] \times [-4, 4]$, and the temporal domain is $t \in [0, 4]$. This problem has an analytical solution:

$$u(t, x, y) = -\tanh\left(\frac{y}{2} \cos(\omega t) - \frac{x}{2} \sin(\omega t)\right) \quad (31)$$

where $\omega = v_t / (r v_{t,\max})$. The initial and boundary conditions are extracted directly from the analytical solution.

Methods are evaluated on a structured 256×256 grid with the same temporal discretization as in the previous section. The governing equations and boundary conditions are specified consistently for FDTO, SPINN, and PINN. For a fair comparison, solution fields are sampled on an identical spatiotemporal grid, and the analytical solution is used as the reference.

Fig. 19 compares the solution fields and absolute error maps at $t = 0, 2$, and 4 for a nonlinear advection problem featuring strong rotational deformation and interface stretching. FDTO accurately captures the spiral mixing structures and remains in close agreement with the reference across all snapshots, with errors primarily confined to the thin spiral interface where gradients are strongest and negligible in the bulk region. SPINN reproduces the main mixing pattern but exhibits slight smoothing in strongly deformed regions, leading to moderate interface-localized errors. By comparison, PINN shows pronounced numerical diffusion and interface distortion, especially at later times, with substantially larger and more scattered errors around the vortex core and along the mixing interface.

To complement the qualitative comparisons in the solution and error contours, Tab. 8 summarizes the quantitative results, reporting the relative L_2 errors together with GPU memory consumption. FDTO achieves the lowest error at $t = 0$ and maintains its advantage as the mixing evolves. At $t = 2$, FDTO attains a relative error of 0.014, which is nearly three times smaller than SPINN and about five times smaller than PINN. Similar trends persist at $t = 4$. In terms of resource usage, SPINN is the most memory efficient, while FDTO requires slightly more GPU memory but remains lightweight and practical. In contrast, PINN consumes roughly twice the GPU memory of FDTO. The proposed solver achieves a favorable balance between solution fidelity and memory efficiency.

Table 8: Comparison of relative L_2 error and GPU memory for the flow mixing problem on a 256×256 grid.

Method	relative L_2 error			GPU memory (MB)
	$t = 0$ s	$t = 2$ s	$t = 4$ s	
SPINN	0.010	0.040	0.045	570
PINN	0.022	0.068	0.066	1590
FDTO	0.009	0.014	0.023	670

3.6. Ablation Studies

3.6.1. Convergence Comparison

Beyond optimization-based baselines, FDTO is further compared with a conventional explicit time-marching finite-

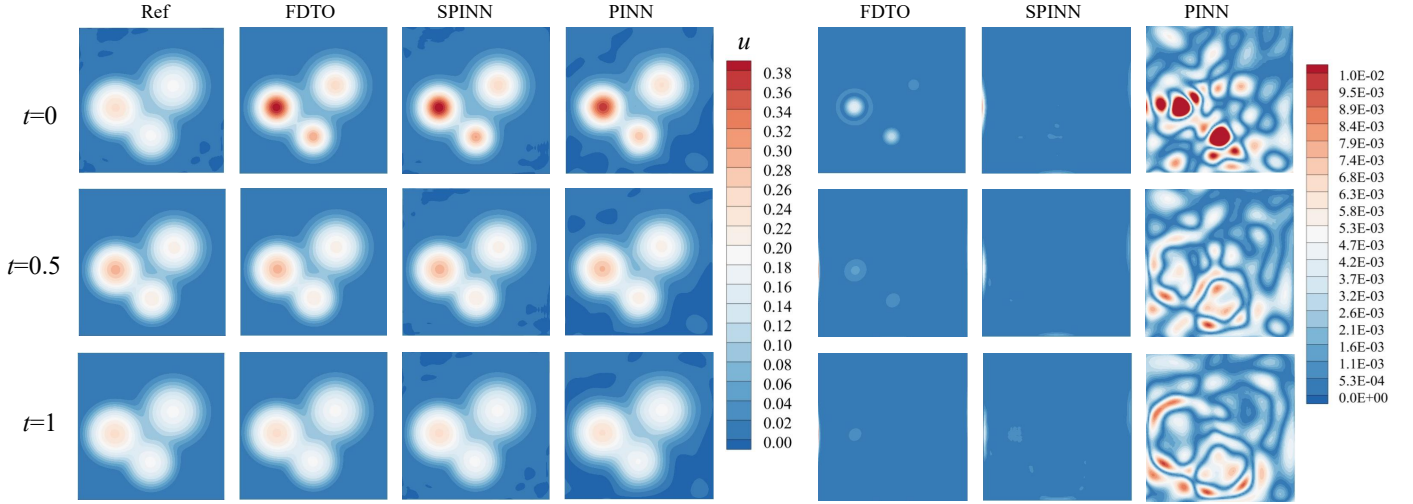


Figure 18: Comparison of flow field (left) and absolute error (right) for diffusion equation on a 101×101 grid.

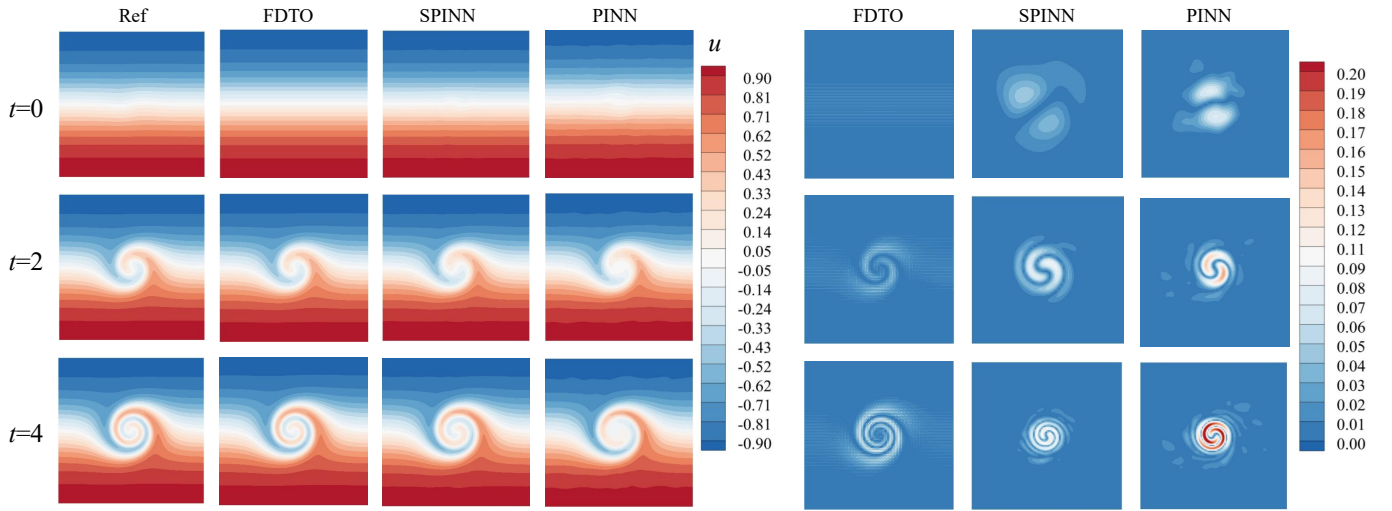


Figure 19: Comparison of flow field (left) and absolute error (right) for flow mixing problem on a 256×256 grid.

volume(ETM-FVM) solver to highlight the benefit of alleviating Courant-Friedrichs-Lewy(CFL) limited updates (Fripp). Fig. 20 presents the convergence histories of the proposed FDTO solver and a ETM-FVM solver for the lid-driven cavity at $Re = 2500$ and $Re = 3200$. In both cases, the ETM-FVM advances the flow field using an explicit update with a CFL limited time step chosen to be the largest empirically stable value, whereas FDTO performs optimization-driven time marching by directly minimizing the discrete residual. The results demonstrate that FDTO reaches a low-error plateau within roughly 200-300 iterations with smooth and nearly monotonic decay, while the ETM-FVM exhibits much slower error reduction and remains at a substantially higher relative L_2 error under the same iteration budget. As the Reynolds number increases, the convergence turning point of FDTO is mildly delayed and the plateau error increases slightly. Nevertheless, FDTO converges markedly faster than the explicit ETM-FVM across all cases, indicating improved efficiency by alleviating the time-step stability constraints inherent to explicit time-marching schemes.

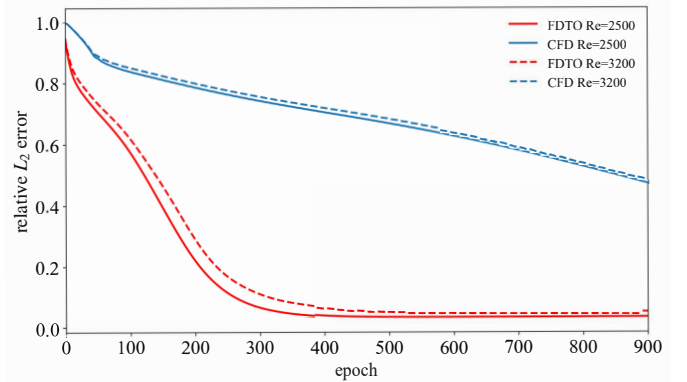


Figure 20: Comparison of FDTO and an explicit time-marching finite-volume solver (ETM-FVM) on a 201×201 lid-driven cavity grid: relative L_2 error versus epoch at $Re = 2500$ and $Re = 3200$.

3.6.2. Inner-Iteration Study

This subsection investigates the sensitivity of FDTO to the number of inner optimization steps per epoch (i.e., per outer time-marching update). As shown in Fig. 21, the impact of the inner-iteration budget is strongly case-dependent. For the diffusion and flow mixing problem, the three curves nearly overlap: increasing inner iterations from 10 to 1000 yields only marginal changes, and the relative L_2 error follows a similar trend as epochs progress (from nearly 4×10^{-3} to 5×10^{-3} for diffusion, and from 10^{-2} to 2.3×10^{-2} for flow mixing), indicating that the overall error is primarily governed by the outer update and discretization rather than insufficient inner solves.

In contrast, the lid-driven cavity case is highly sensitive to inner iterations: with only 10 inner steps, the error decreases slowly and remains large even after 2000 epochs, whereas 100 or 1000 inner steps produce a rapid error drop and reach a low-error plateau around 5×10^{-2} , with 1000 iterations converging noticeably faster in the early stage but attaining a similar final level as 100 iterations (diminishing returns).

For the NACA0012 case, 100 inner iterations improves convergence over 10 iterations and reaches a lower steady error level. In contrast, 1000 inner iterations becomes unstable: after an initially rapid decrease, the error gradually increases and eventually diverges. This behavior suggests that an overly aggressive inner-iteration budget can destabilize the coupled outer update in a more nonlinear, geometry-influenced setting.

These results indicate a practical trade-off. Increasing the inner-iteration budget can substantially accelerate convergence when inner under-optimization is the main bottleneck (e.g., the lid-driven cavity case), but it offers limited benefit when convergence is dominated by the outer update (diffusion/mixing) and may even reduce robustness (NACA0012). A moderate choice (e.g., 100) provides a favorable balance among accuracy, computational cost, and stability across the tested cases.

3.6.3. Effect of Time-step Size

The influence of the outer time-step size Δt on FDTO convergence is also investigated. Fig. 22 reports the relative L_2 error histories for $\Delta t \in \{0.01, 0.05, 0.1\}$ under the same optimization configuration.

For the lid-driven cavity at $Re = 2500$, increasing Δt yields faster and deeper error reduction. With $\Delta t = 0.1$, the error decays nearly monotonically, reaches 10^{-2} within a few hundred epochs, and then remains on a low plateau. By comparison, $\Delta t = 0.05$ converges more slowly and levels off at a higher error, while $\Delta t = 0.01$ shows only marginal improvement over 600 epochs and stays above 10^{-1} . These trends suggest that an overly small Δt leads to under-updated outer steps and consequently slow practical convergence for this case.

For the NACA0012 case ($Re = 100$, $\alpha = 15^\circ$), the trend is reversed. While $\Delta t = 0.01$ and $\Delta t = 0.05$ both yield stable convergence to a low-error regime (around 10^{-2}) after the rapid initial drop in the error, the large step size $\Delta t = 0.1$ becomes unstable: despite an early decrease, the error gradually increases and eventually grows to a significantly higher level. This indicates that, an overly aggressive outer update can overshoot the

stable descent region and amplify discretization/coupling errors in the optimization-driven update.

Fig. 22 reveals a robustness-speed trade-off in selecting Δt . Larger Δt can accelerate convergence when the dynamics are relatively well behaved (e.g., the lid-driven cavity), but it may reduce stability for more challenging cases (e.g., airfoil flow). In practice, a moderate or smaller Δt is often preferable for robustness, and an adaptive schedule that decreases Δt over the optimization can balance early-stage speed with late-stage stability.

3.6.4. Optimizer selection

Three optimizers (Adam, L-BFGS, and SOAP) are compared for minimizing the discrete loss under identical discretization, optimization settings, and stopping criteria. For each case, the relative L_2 error of the predicted solution is tracked against the corresponding reference (analytical/CFD) solution as optimization proceeds.

Fig. 23 shows that optimizer behavior is strongly problem dependent. For the diffusion and flow mixing problem, L-BFGS consistently maintains the lowest error throughout training, indicating that quasi-Newton updates are effective for these smooth objectives and can better control error growth over epochs. For the lid-driven cavity case, all optimizers reduce the error, but L-BFGS converges faster and reaches a lower final plateau, while Adam converges more slowly and Soap exhibits a higher-error saturation, suggesting reduced effectiveness when the optimization becomes increasingly stiff in later epochs. In contrast, for the NACA0012 case, Adam and Soap rapidly drive the error down to a low level within the early epochs, whereas L-BFGS stalls at a substantially higher error.

No single optimizer dominates across all regimes: L-BFGS is highly competitive on smooth PDE cases and the lid-driven cavity flow, while adaptive first-order methods (Adam) and preconditioned variants (Soap) are more robust for the airfoil case.

3.6.5. Grid-Resolution Study

A grid-resolution study is conducted to assess the sensitivity of FDTO to spatial discretization and the robustness of its convergence across mesh sizes. Fig. 24 reports the relative L_2 error histories for the lid-driven cavity at $Re = 2500$ on 151×151 , 201×201 , 251×251 , and 301×301 grids. Across all resolutions, the error decreases smoothly and transitions into a stable plateau, indicating robust convergence with respect to mesh refinement. The convergence behavior, however, exhibits a clear accuracy-effort trade-off: coarser grids reduce the error more rapidly in the early stage but settle at higher plateau levels, whereas finer grids require more epochs to reach the turning point yet achieve lower final errors. These trends suggest that higher resolutions expose richer small-scale features and stricter residual consistency, which increases optimization difficulty; stronger optimization settings (e.g., larger inner-iteration budgets or adaptive schedules) can therefore be beneficial to fully realize the accuracy gains on refined meshes.

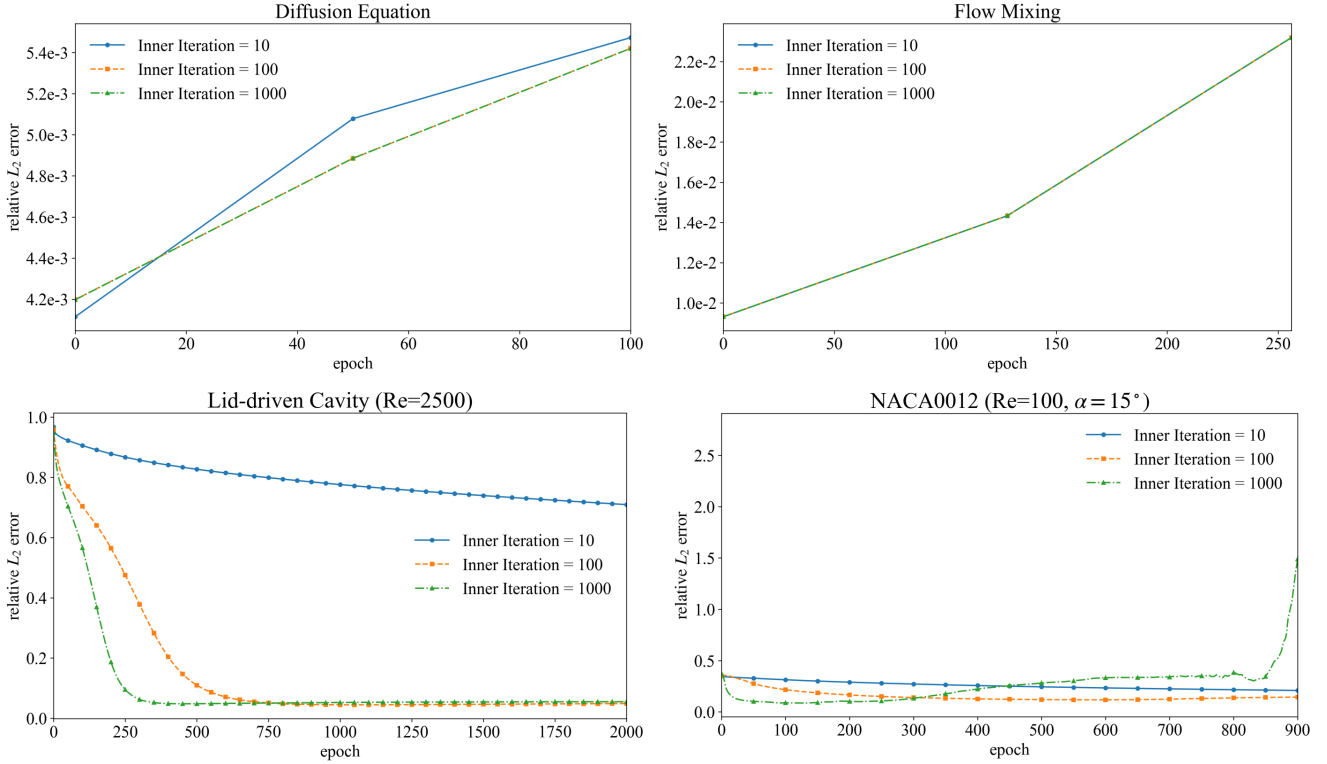


Figure 21: Comparison of inner iterations on convergence across four cases: diffusion equation, flow mixing problem, lid-driven cavity ($Re = 2500$) and NACA0012 ($Re = 100$, $\alpha = 15^\circ$).

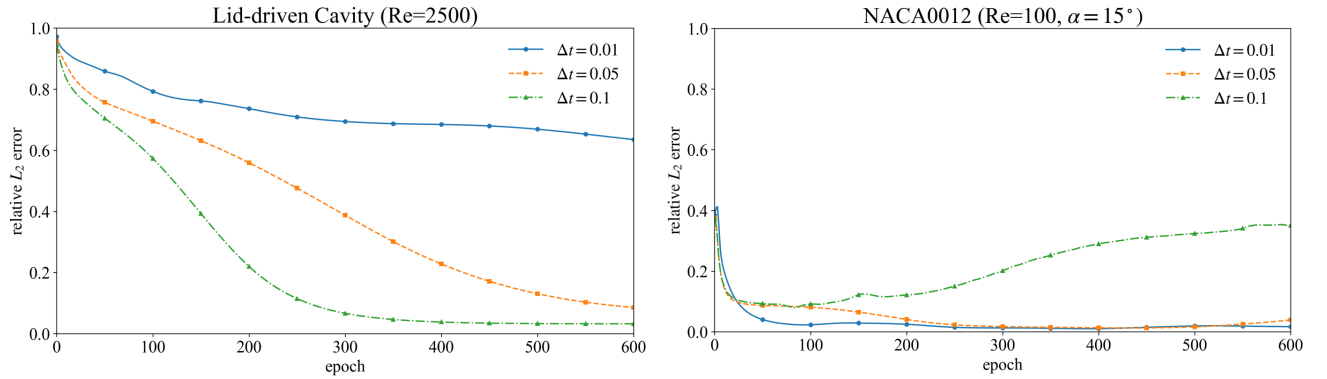


Figure 22: Effect of time-stepping choice ($\Delta t=0.1, 0.05, 0.01$) on lid-driven cavity ($Re = 2500$), and NACA0012 ($Re = 100$, $\alpha = 15^\circ$).

3.6.6. Time-Stepping Ablation

The impact of the proposed time-stepping (TS) optimization on stability and temporal coherence is assessed within the optimization-driven time-marching procedure. As shown in Fig. 25 for the lid-driven cavity at $Re = 2500$ on a 201×201 grid, the velocity-magnitude contours (top row) recover the dominant recirculation pattern in both settings; the absolute error maps (bottom row), however, reveal pronounced differences. With TS enabled, errors remain uniformly small and spatially smooth, whereas disabling TS leads to substantially larger and more structured discrepancies, including a distinct high-error band around the primary vortex and amplified errors near wall-adjacent shear layers. This advantage is further quan-

tified by the convergence histories: Fig. 26 shows that the time-marching formulation converges faster and attains lower errors than the time-independent variant. These results indicate that incorporating temporal dynamics improves optimization stability and helps resolve nonlinear flow structures. TS therefore serves as an effective stabilization mechanism, enforcing temporally consistent evolution, reducing oscillatory updates during time marching, and improving robustness and accuracy in convection-dominated, high-Reynolds-number regimes.

3.6.7. Ablation of N-C-N Stabilization

The effect of the N-C-N averaging treatment on suppressing spurious oscillations in convection-dominated regimes is

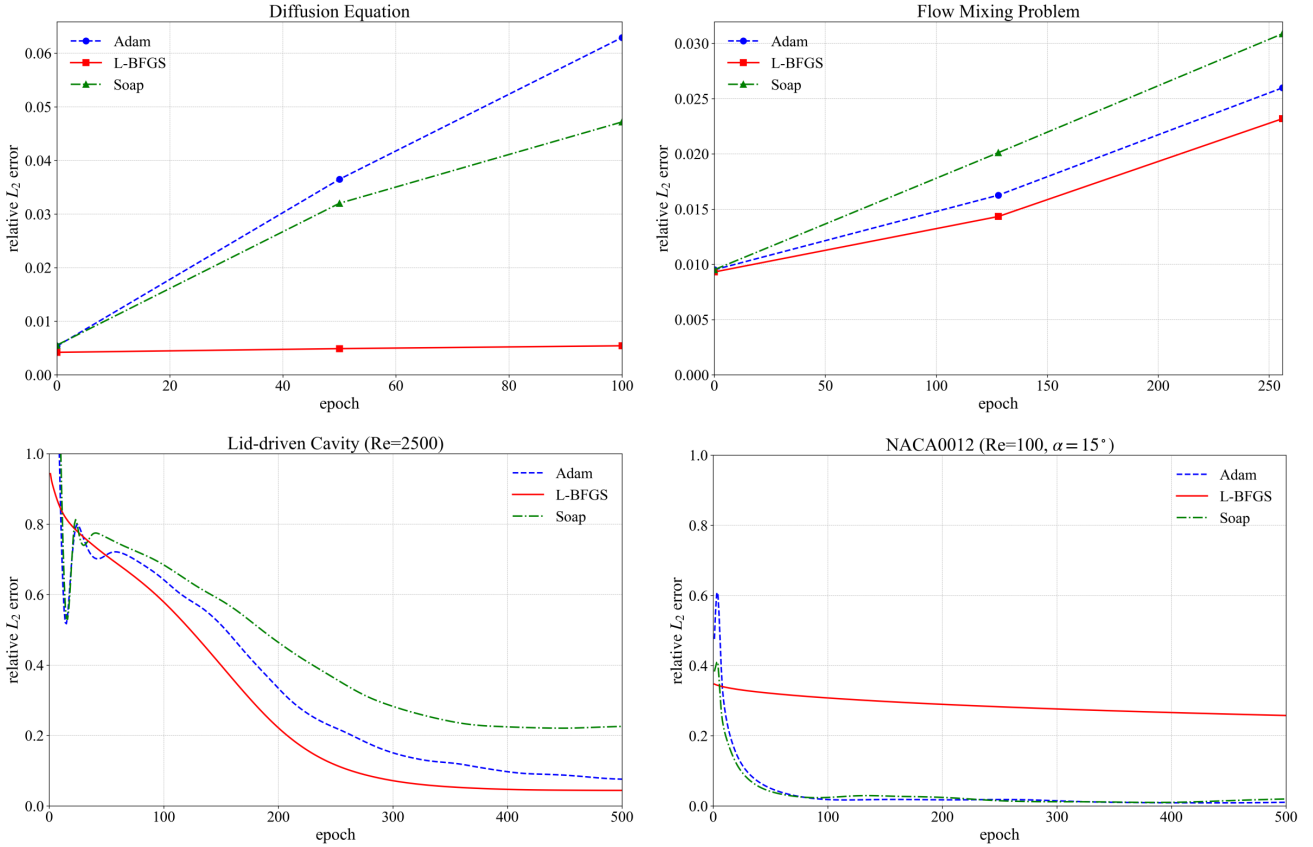


Figure 23: Effect of optimizer choice (Adam, L-BFGS, and Soap) across four cases: diffusion equation, flow mixing problem, lid-driven cavity ($Re = 2500$), and NACA0012 ($Re = 100$, $\alpha = 15^\circ$).

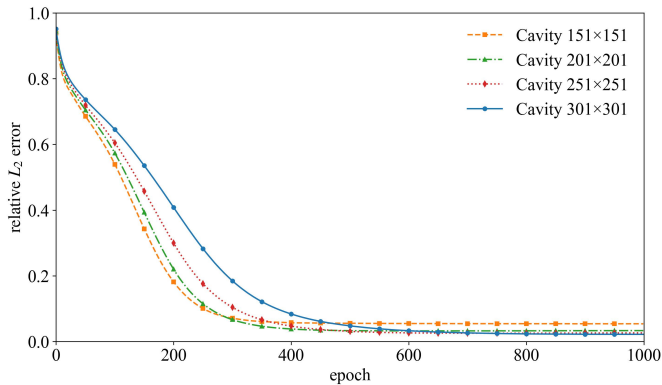


Figure 24: Grid-resolution study for lid-driven cavity flow at $Re = 2500$: relative L_2 error versus epoch on 151×151 , 201×201 , 251×251 , and 301×301 grids.

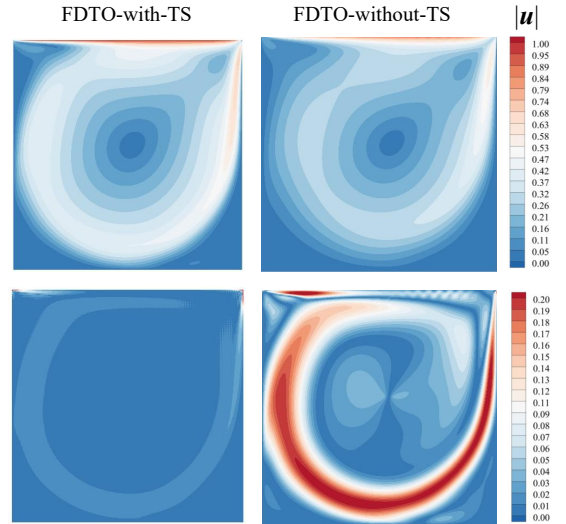


Figure 25: Effect of TS optimization on lid-driven cavity flow at $Re = 2500$ on a 201×201 grid: velocity-magnitude contours (top) and absolute error maps (bottom) for FDTO with and without TS.

assessed next. Fig. 27 shows that, without N-C-N averaging, high-frequency oscillations accumulate during optimization-driven time marching, producing irregular pressure contours and enlarged pressure-error regions near the trailing edge and within the wake. When the N-C-N operator is applied to the discrete state (\mathbf{u}, p) , field regularity improves markedly and pressure errors are substantially reduced across the domain. These results indicate that the lightweight, fully discrete N-C-N stabilization improves optimization stability and strengthens

pressure-reconstruction robustness in wake-dominated flows, consistent with the design rationale discussed in the Introduction.

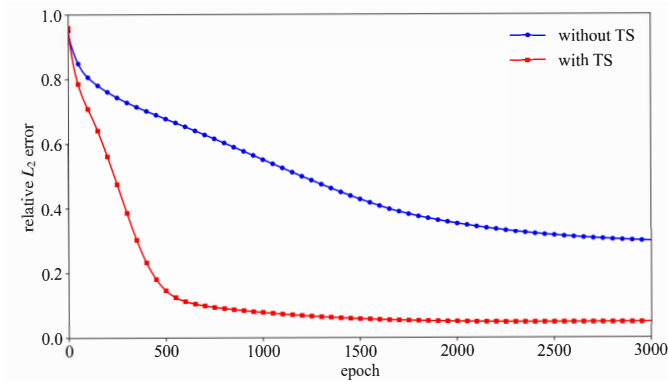


Figure 26: Effect of time-stepping optimization on lid-driven cavity flow at $Re = 2500$ on a 201×201 grid: convergence of relative L_2 error with and without TS.

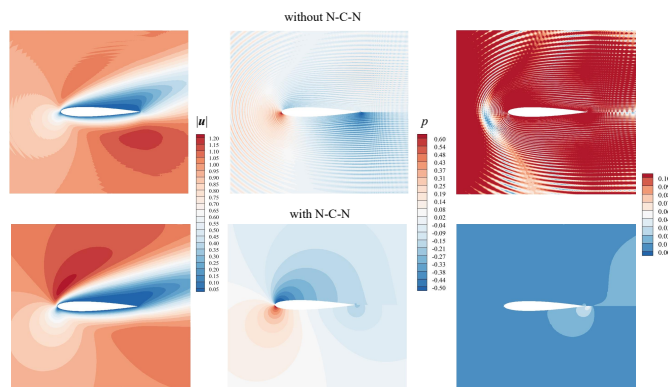


Figure 27: Ablation study of the N-C-N treatment for an airfoil case: comparison of velocity magnitude (left), pressure (middle), and absolute pressure error (right) without (top row) and with (bottom row) N-C-N.

4. Conclusions

This work proposes FDTO, a finite-differentiable, discrete-optimization framework for PDE solving that optimizes the unknown fields directly over discrete degrees of freedom. FDTO combines classical discretizations with an optimization-driven time-marching scheme and incorporates a lightweight, fully discrete smoothing treatment to suppress error accumulation in convection-dominated regimes. As a result, the method improves convergence stability while retaining geometric adaptability on body-fitted grids.

Sec. 3 demonstrates the effectiveness of FDTO primarily on incompressible Navier-Stokes problems, including lid-driven cavity flows across a wide Reynolds-number range, external airfoil aerodynamics, and a cylinder wake on a multi-block structured grid. Diffusion and nonlinear mixing are also included to illustrate broader applicability. Across these settings, FDTO delivers accurate field predictions with smooth, stable convergence and substantially lower GPU memory usage than representative neural solvers. Moreover, it maintains robust pressure reconstruction in wake-dominated regions and preserves cross-block coherence without interface-aligned artifacts. Collectively, these results suggest that FDTO provides a practical route for solving convection-dominated flows and other PDEs

through a purely discrete optimization formulation.

Several limitations remain. Optimization becomes more demanding on finer grids, motivating grid-consistent normalization/weighting and continuation strategies such as coarse-to-fine initialization. Extending the framework to higher-Reynolds-number regimes and fully three-dimensional geometries will likely require stronger stabilization and preconditioning, together with scalable parallel implementations. Addressing these challenges is an important direction toward large-scale, engineering-grade applications.

Author contributions

CRedit: Yali Luo: Investigation, Methodology, Software, Validation, Visualization, Writing-original draft; Yiye Zou: Investigation, Methodology, Software; Heng Zhang: Validation, Visualization; Mingjie Zhang: Writing review & editing; Gang Wei: Writing review & editing; Jingyu Wang: Funding acquisition, Resources, Supervision, Writing-review & editing; Xiaogang Deng: Project administration, Writing-review & editing

Disclosure statement

No potential conflict of interest was reported by the author(s).

Funding

This research is funded by the Sichuan Science and Technology Program (Project No.2021ZDZX0001), the Open Funding of National key laboratory of Fundamental Algorithms and Models for Engineering Simulation, and the Sichuan University Interdisciplinary Innovation Fund.

Data availability statement

The code and grid used in this paper can be found in the GitHub repository: https://github.com/My-git96/FDTO_PDE

Declaration of generative AI and AI-assisted technologies in the writing process

During the preparation of this work the author(s) used ChatGPT in order to improve phrasing. After using this tool/service, the author(s) reviewed and edited the content as needed and take(s) full responsibility for the content of the publication.

References

Bar-Sinai, Y., Hoyer, S., Hickey, J., Brenner, M.P., 2019. Learning data-driven discretizations for partial differential equations. *Proceedings of the National Academy of Sciences* 116, 15344–15349.

- Baydin, A.G., Pearlmutter, B.A., Radul, A.A., Siskind, J.M., 2018. Automatic differentiation in machine learning: a survey. *Journal of machine learning research* 18, 1–43.
- Bettencourt, J., Johnson, M.J., Duvenaud, D., 2019. Taylor-mode automatic differentiation for higher-order derivatives in jax, in: *Program Transformations for ML Workshop at NeurIPS 2019*.
- Bhatia, S., Dangel, F., 2024. Lowering pytorch’s memory consumption for selective differentiation, in: *Proceedings of the IEEE/CVF Conference on Computer Vision and Pattern Recognition*, pp. 8260–8265.
- Blazek, J., 2015. *Computational fluid dynamics: principles and applications*. Butterworth-Heinemann.
- Buhendwa, A.B., Bezgin, D.A., Karnakov, P., Adams, N.A., Koumoutsakos, P., 2025. Data-driven shape inference in three-dimensional steady-state supersonic flows: Optimizing a discrete loss with jax-fluids. *Physical Review Fluids* 10, 084902.
- CAO, D., LI, Q., XU, Y., Yu, F., 2025. A promotion approach for digital construction in the equipment field. *Gas Turbine Experiment and Research* 38, 118–122.
- Cao, W., Tang, S., Ma, Q., Ouyang, W., Zhang, W., 2025. A surrogate model based on parametric neural network solvers for laminar flows around aerofoils. *Engineering Applications of Computational Fluid Mechanics* 19, 2559110.
- Cao, W., Zhang, W., 2025a. An analysis and solution of ill-conditioning in physics-informed neural networks. *Journal of Computational Physics* 520, 113494.
- Cao, W., Zhang, W., 2025b. Overcoming the loss conditioning bottleneck in optimization-based pde solvers: A novel well-conditioned loss function. *arXiv preprint arXiv:2508.02692*.
- Chen, R., Wang, S., Wang, S., Cai, J., 2024a. Separation and reattachment fixed reynolds-stress model for iced airfoil and wing simulations. *Aerospace Science and Technology* 155, 109587.
- Chen, X., Wang, Z., Deng, L., Yan, J., Gong, C., Yang, B., Wang, Q., Zhang, Q., Yang, L., Pang, Y., et al., 2024b. Towards a new paradigm in intelligence-driven computational fluid dynamics simulations. *Engineering Applications of Computational Fluid Mechanics* 18, 2407005.
- Chiu, P.H., Wong, J.C., Ooi, C., Dao, M.H., Ong, Y.S., 2022. Can-pinn: A fast physics-informed neural network based on coupled-automatic-numerical differentiation method. *Computer Methods in Applied Mechanics and Engineering* 395, 114909.
- Cho, J., Nam, S., Yang, H., Yun, S.B., Hong, Y., Park, E., 2023. Separable physics-informed neural networks. *Advances in Neural Information Processing Systems* 36, 23761–23788.
- Crank, J., Nicolson, P., 1947. A practical method for numerical evaluation of solutions of partial differential equations of the heat-conduction type, in: *Mathematical proceedings of the Cambridge philosophical society*, Cambridge University Press. pp. 50–67.
- Fripp, K., . Finite-volume-cfd-in-matlab: A 2d time-dependent cfd solver in matlab using a staggered grid and non-uniform cartesian meshes. GitHub repository. URL: <https://github.com/KevinGFripp/Finite-Volume-CFD-in-MATLAB>.
- Gao, H., Zahr, M.J., Wang, J.X., 2022. Physics-informed graph neural galerkin networks: A unified framework for solving pde-governed forward and inverse problems. *Computer Methods in Applied Mechanics and Engineering* 390, 114502.
- Ghia, U., Ghia, K.N., Shin, C., 1982. High-re solutions for incompressible flow using the navier-stokes equations and a multigrid method. *Journal of computational physics* 48, 387–411.
- Gunes Baydin, A., Pearlmutter, B.A., Andreyevich Radul, A., Siskind, J.M., 2015. Automatic differentiation in machine learning: a survey. *arXiv e-prints*, arXiv-1502.
- Karnakov, P., Litvinov, S., Koumoutsakos, P., 2023. Flow reconstruction by multiresolution optimization of a discrete loss with automatic differentiation. *The European Physical Journal E* 46, 59.
- Karnakov, P., Litvinov, S., Koumoutsakos, P., 2024. Solving inverse problems in physics by optimizing a discrete loss: Fast and accurate learning without neural networks. *PNAS nexus* 3, pgae005.
- Kingma, D.P., 2014. Adam: A method for stochastic optimization. *arXiv preprint arXiv:1412.6980*.
- LeVeque, R.J., 2007. *Finite difference methods for ordinary and partial differential equations: steady-state and time-dependent problems*. SIAM.
- Li, T., Zou, S., Chang, X., Zhang, L., Deng, X., 2024. Predicting unsteady incompressible fluid dynamics with finite volume informed neural network. *Physics of Fluids* 36.
- Li, T., Zou, Y., Zou, S., Chang, X., Zhang, L., Deng, X., 2025. Learning to solve pdes with finite volume-informed neural networks in a data-free approach. *Journal of Computational Physics* 530, 113919.
- Lu, L., Su, J., Wang, J., Deng, X., 2026. Ampinn: anisotropic and multiscale cross-attention physics-inspired neural networks for turbulence prediction. *Engineering Applications of Computational Fluid Mechanics* 20, 2628951.
- Lu, L., Zou, Y., Wang, J., Zou, S., Zhang, L., Deng, X., 2025. Unsupervised learning with physics informed graph networks for partial differential equations: L. lu et al. *Applied Intelligence* 55, 617.

- Moukalled, F., Mangani, L., Darwish, M., 2015. The finite volume method, in: *The finite volume method in computational fluid dynamics: An advanced introduction with OpenFOAM® and Matlab*. Springer, pp. 103–135.
- Raissi, M., Perdikaris, P., Karniadakis, G.E., 2019. Physics-informed neural networks: A deep learning framework for solving forward and inverse problems involving nonlinear partial differential equations. *Journal of Computational physics* 378, 686–707.
- Rao, C., Sun, H., Liu, Y., 2020. Physics-informed deep learning for incompressible laminar flows. *Theoretical and Applied Mechanics Letters* 10, 207–212.
- Reddy, J.N., 1993. *An introduction to the finite element method*. New York 27.
- Sanchez-Gonzalez, A., Godwin, J., Pfaff, T., Ying, R., Leskovec, J., Battaglia, P., 2020. Learning to simulate complex physics with graph networks, in: *International conference on machine learning*, PMLR. pp. 8459–8468.
- Temam, R., 2024. *Navier–Stokes equations: theory and numerical analysis*. volume 343. American Mathematical Society.
- Thuerey, N., Weißenow, K., Prantl, L., Hu, X., 2020. Deep learning methods for reynolds-averaged navier–stokes simulations of airfoil flows. *AIAA journal* 58, 25–36.
- Vyas, N., Morwani, D., Zhao, R., Kwun, M., Shapira, I., Brandfonbrener, D., Janson, L., Kakade, S., 2024. Soap: Improving and stabilizing shampoo using adam. *arXiv preprint arXiv:2409.11321* .
- Wang, S., Deng, X., Wang, G., Yang, X., 2020. Blending the eddy-viscosity and reynolds-stress models using uniform high-order discretization. *AIAA Journal* 58, 5361–5378.
- Wang, S., Dong, Y., Deng, X., Wang, G., Wang, J., 2018. High-order simulation of aeronautical separated flows with a reynold stress model. *Journal of Aircraft* 55, 1177–1190.
- Wang, Z., Meng, X., Jiang, X., Xiang, H., Karniadakis, G.E., 2023. Solution multiplicity and effects of data and eddy viscosity on navier-stokes solutions inferred by physics-informed neural networks. *arXiv preprint arXiv:2309.06010* .
- ZENG, J., ZHANG, J., 2025. Application of computational fluid dynamics in aero-engine development. *Gas Turbine Experiment and Research* 38, 58–72.
- Zhu, C., Byrd, R.H., Lu, P., Nocedal, J., 1997. Algorithm 778: L-bfgs-b: Fortran subroutines for large-scale bound-constrained optimization. *ACM Transactions on mathematical software (TOMS)* 23, 550–560.
- Zou, Y., Li, T., Lu, L., Wang, J., Zou, S., Zhang, L., Deng, X., 2024. Finite-difference-informed graph network for solving steady-state incompressible flows on block-structured grids. *Physics of Fluids* 36.